Contributions to Mineralogy and Petrology (2019) 174:58
https://doi.org/10.1007/s00410-019-1592-4

ORIGINAL PAPER

H_2O–CO_2 solubility in alkali-rich mafic magmas: new experiments at mid-crustal pressures

Chelsea M. Allison[1,2] · **Kurt Roggensack**[1] · **Amanda B. Clarke**[1,3]

Received: 27 March 2018 / Accepted: 4 June 2019

Abstract

Volatile solubility in magmas depends on several factors, including composition and pressure. Mafic magmas with high concentrations of alkali elements are capable of dissolving larger quantities of H_2O and CO_2 than subalkaline basalt, which possibly contributes to large explosive eruptions. Existing volatile solubility models for alkali-rich mafic magmas are well calibrated below ~ 200 MPa, but at greater pressures the experimental data are sparse. To fill in this gap, we conducted a set of mixed H_2O–CO_2 volatile solubility experiments between 400 and 600 MPa at 1200 °C in six mafic compositions with variable alkali contents (Stromboli, Etna, Vesuvius, Erebus, Sunset Crater, and the San Francisco Volcanic Field). Results from our experiments indicate that existing volatile solubility models for alkali-rich mafic magmas, if extrapolated beyond their calibrated ranges, do not accurately describe CO_2 solubility at mid-crustal pressures. We adapt an existing thermodynamic model to reflect our higher-pressure experimental data by determining model parameters $\Delta V_r^{0,m}$ (partial molar volume change of CO_2 reaction) and K_0 (equilibrium constant) for each studied composition. In these compositions, $\Delta V_r^{0,m}$ is found to vary between ~ 15 and ~ 25 $cm^3\ mol^{-1}$, while ln K_0 ranges from − 14.9 to − 14.0. The calculated solubility curves show good agreement with CO_2 solubility data from the experiments and provide a more accurate description of CO_2 solubility than purely empirical fits. These new experiments indicate while CO_2 solubility is increased in alkali-rich mafic magmas, it is not simply controlled by total alkali content but rather the full multicomponent magma composition.

Keywords Volatile solubility · Basaltic explosive volcanism · Alkali basalts · Stromboli · Etna · Erebus

Introduction

The style and scale of volcanic eruptions are in part controlled by the type and amount of volatile components in the magmatic system (e.g., Sparks 1978; Wilson 1980). Volatiles affect the dynamics of the volcanic system, from magma storage and evolution to ascent and eruption or degassing (e.g., Sparks 1978; Wilson 1980; Newman and Lowenstern 2002; Lesne et al. 2011b). Volatile solubility directly influences magmatic processes such as the timing of volatile exsolution and its effect on the bulk properties of the magma (e.g., Spera and Bergman 1980; Holloway and Blank 1994; Dixon and Stolper 1995; Manga et al. 1998), including crystallization (e.g., Moore and Carmichael 1998). Dissolved volatiles affect magmatic density and viscosity (e.g., Hess and Dingwell 1996; Ochs and Lange 1999), while bubbles formed from exsolved volatiles may regulate overall eruptive style (Sparks 1978; Wilson 1980; Wilson et al. 1980). For example, volatiles exsolving from a slow-rising basaltic magma can decouple from the liquid, resulting in degassed lava flows or relatively small explosions from gas slugs (e.g., Blackburn et al. 1976; Wilson and Head 1981). Alternatively, abundant volatiles trapped in a rapidly ascending magma can produce hazardous sub-Plinian to Plinian eruptions (e.g., Wilson 1980; Walker 1993).

Communicated by Mark S Ghiorso.

Electronic supplementary material The online version of this article (https://doi.org/10.1007/s00410-019-1592-4) contains supplementary material, which is available to authorized users.

✉ Chelsea M. Allison
cmalliso@asu.edu

[1] School of Earth and Space Exploration, Arizona State University, PO Box 876004, Tempe, AZ 85287-6004, USA

[2] Present Address: Department of Earth and Atmospheric Sciences, Cornell University, Snee Hall, Room 2122, Ithaca, NY 14853, USA

[3] Istituto Nazionale di Geofisica e Vulcanologia, Sezione di Pisa, Italy

Published online: 14 June 2019

Magmatic volatile contents can be constrained in a variety of ways, including by investigation of melt inclusions trapped in crystals growing in the magma at depth (e.g., Lowenstern 1995). When combined with knowledge of volatile solubility, melt inclusion volatile concentrations can be used to calculate entrapment pressures and therefore provide constraints on the magma plumbing system and the path to eruption (e.g., Lowenstern 1995; Holloway and Blank 1994; Dixon and Stolper 1995; Métrich et al. 2010). The composition of these volatiles can also affect eruptive dynamics. The volatile budget in a basaltic magma is primarily composed of water (H_2O) and carbon dioxide (CO_2), with water being the most abundant species (e.g., Holloway 1981; Blank and Brooker 1994). However, CO_2 is much less soluble than water (e.g., Wyllie and Tuttle 1959; Holloway and Blank 1994) and consequently makes up the bulk of the exsolved gas at depths greater than a few kilometers. CO_2 solubility therefore plays a very important role in initiating the ascent and eruption of basaltic magmas.

Volatile solubility in magmas is strongly compositionally dependent. One control on overall volatile solubility is thought to be silica content (e.g., Holloway and Blank 1994; Newman and Lowenstern 2002). Nevertheless, mafic magmas with similar silica contents can exhibit drastically different volatile solubilities, the cause of which is primarily correlated to varied concentrations of alkali elements (e.g., Holloway and Blank 1994). Dixon (1997) described H_2O–CO_2 solubility in alkali-rich basaltic magmas based on a parameterization of the different elements in a magma composition. This model was developed using previously published datasets of mixed H_2O–CO_2 experiments conducted between 100 MPa and 2 GPa for four mafic compositions with a range of silica and alkali contents (Pan et al. 1991; Thibault and Holloway 1994; Holloway and Blank 1994; Dixon and Pan 1995; Dixon et al. 1995). The resulting compositional parameter Π was defined such that compositions with a greater Π value should have higher CO_2 solubility. Experimental work on mixed H_2O–CO_2 solubility in alkali-rich mafic magmas continued over the years to incorporate more compositions across a large pressure range, including studies by Botcharnikov et al. (2005a), Behrens et al. (2009), Pichavant et al. (2009), Lesne et al. (2011a, b), Iacono-Marziano et al. (2012), Iacovino et al. (2013), Pichavant et al. (2014), Shishkina et al. (2014), Vetere et al. (2014), and Iacovino et al. (2016) (Fig. 1). Notably, the three compositions studied by Lesne et al. (2011b) had varying alkali contents but were fairly similar in other major elements, and yet their CO_2 solubilities did not uniformly correlate with their Π values. This lack of obvious correlation suggests that in a narrow compositional range, Π may not explain all observed differences in CO_2 solubility.

There are some pressure ranges for which the existing experimental data for H_2O–CO_2 solubility in alkali-rich mafic magmas is sparse. Figure 1 shows the total alkali content and experiment pressure of mixed H_2O–CO_2 solubility

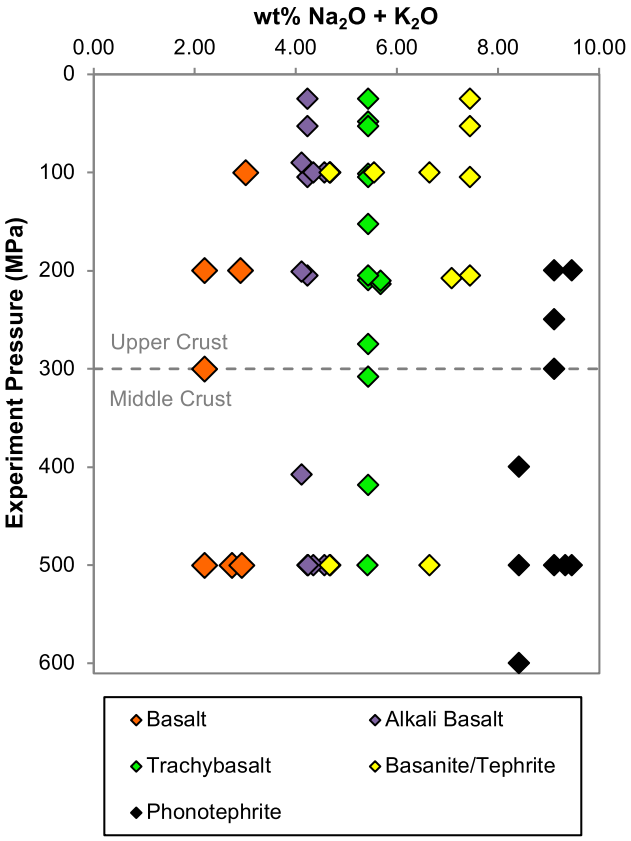

Fig. 1 Previously published mixed H_2O–CO_2 volatile solubility experiments in alkali-rich mafic magmas, plotted as the pressure and alkali content of experiments. Subalkaline basalts that have been incorporated into models for alkali basalts are also included. Experiments shown are from the following studies: Pan et al. (1991), Thibault and Holloway (1994), Holloway and Blank (1994), Dixon et al. (1995), Botcharnikov et al. (2005a), Behrens et al. (2009), Pichavant et al. (2009), Lesne et al. (2011a, b), Iacono-Marziano et al. (2012), Iacovino et al. (2013), Pichavant et al. (2014), Shishkina et al. (2014), Vetere et al. (2014), and Iacovino et al. (2016). Colors indicate classification of the magma compositions according to total alkali and silica content (see Fig. 2)

experiments for alkali-rich mafic magmas. Subalkaline basaltic compositions that have been used to calibrate models for alkali-rich mafic magmas are also included. Note that although the maximum pressure shown in Fig. 1 is 600 MPa, there have been some experiments conducted at higher pressures. As illustrated in Fig. 1, the region encompassing the middle of the crust (~300–600 MPa) is not well represented relative to the upper crust (<300 MPa). For certain basaltic systems, low-pressure experiments (<200 MPa) may provide constraints on volatile solubility sufficient for interpretation of melt inclusion volatile contents. Some explosive basaltic eruptions, however, have CO_2 contents higher than the calibrated limits of existing volatile solubility models (e.g., Sable et al. 2006; Allison 2018).

Additionally, recent work indicates that for some volcanoes, previous analyses and calculations may underestimate

CO_2 content by as much as 90% because significant CO_2 sequesters into vapor bubbles within the melt inclusions during cooling (e.g., Hartley et al. 2014; Moore et al. 2015; Aster et al. 2016). The behavior of CO_2 at high pressure (indicated by high CO_2 contents) is complicated to model because its behavior is non-ideal (e.g., Holloway and Blank 1994). For example, while the fugacity of pure H_2O at 1200 °C and 400 MPa is only tens of MPa greater than the pressure, the fugacity of pure CO_2 at these conditions is > 1000 MPa, and this gap between pressure and CO_2 fugacity continues to widen with increased pressure (Holloway 1981, 1987; Holloway and Blank 1994). Another driver for additional CO_2 datasets is the fact that CO_2 appears to be more sensitive than water is to the compositional variability of alkali-rich mafic magmas (e.g., Holloway and Blank 1994; Dixon 1997; Lesne et al. 2011a, b).

To improve understanding of CO_2 solubility in alkali-rich mafic compositions at mid-crustal pressures, we have conducted a new set of mixed H_2O–CO_2 volatile solubility experiments. We studied a range of alkali-rich mafic compositions through experiments run at 1200 °C between 400 and 600 MPa. While CO_2 was the focus of this work for the reasons previously mentioned, we performed mixed H_2O–CO_2 experiments to appropriately consider solubility in natural systems that typically contain both fluids. We calculate empirical and thermodynamic fits for CO_2 solubility and use this new solubility data to better understand what affects and controls CO_2 solubility in alkali-rich mafic magmas.

Experimental techniques

Starting material

Six different basaltic compositions with variable alkali content were studied (Table 1; Fig. 2). Compositions include alkali basalts from Sunset Crater (AZ, USA) and

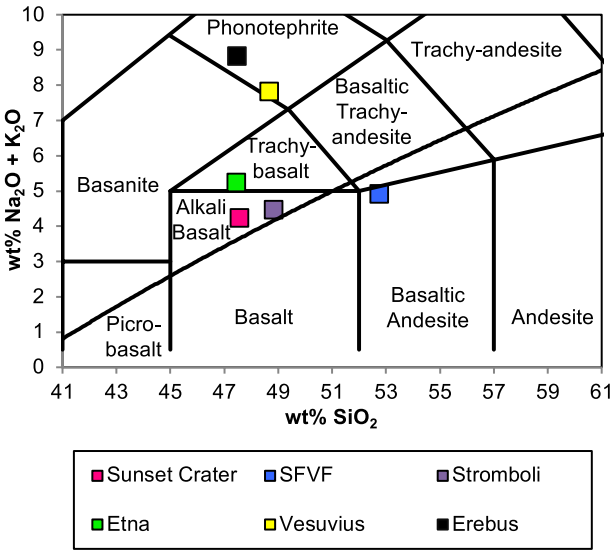

Fig. 2 Starting glass compositions on total alkali silica diagram

Table 1 Compositions of starting glasses

Composition	SiO_2	TiO_2	Al_2O_3	FeO[a]	MnO	MgO	CaO	Na_2O	K_2O	P_2O_5	Total	Source
Compositions used in this study												
SFVF	52.77	1.18	17.28	7.88	0.19	5.86	9.19	3.39	1.50	0.76	100	Natural
(*4*)	*0.82*	*0.04*	*0.25*	*0.56*	*0.04*	*0.43*	*0.44*	*0.44*	*0.17*	*0.07*		
Sunset Crater	47.61	1.80	16.22	11.02	0.17	8.66	9.84	3.43	0.80	0.45	100	Natural
(*8*)	*0.87*	*0.06*	*1.20*	*1.02*	*0.02*	*1.58*	*0.25*	*0.22*	*0.07*	*0.06*		
Erebus	47.49	2.79	18.83	10.36	0.29	3.31	6.95	6.03	2.78	1.17	100	Synthesized
(*4*)	*0.36*	*0.05*	*0.60*	*0.37*	*0.03*	*0.31*	*0.29*	*0.09*	*0.12*	*0.06*		
Vesuvius	48.69	0.98	15.26	8.15	0.23	6.68	11.60	1.93	5.86	0.62	100	Synthesized
(*4*)	*0.28*	*0.02*	*0.29*	*0.14*	*0.02*	*0.38*	*0.29*	*0.06*	*0.19*	*0.04*		
Etna	47.46	1.81	16.17	10.47	0.20	6.74	11.42	3.48	1.72	0.52	100	Natural
(*6*)	*0.41*	*0.09*	*1.36*	*0.80*	*0.03*	*0.90*	*0.50*	*0.28*	*0.21*	*0.03*		
Stromboli	48.85	0.83	16.83	8.15	0.20	7.81	12.45	2.46	1.99	0.43	100	Synthesized
(*30*)	*0.54*	*0.02*	*0.67*	*0.33*	*0.02*	*0.54*	*0.43*	*0.13*	*0.15*	*0.05*		
Compositions from Lesne et al. (2011a, b)												
VES-9 (Vesuvius)	48.67	0.97	14.72	7.62	0.14	6.82	12.94	1.82	5.63	0.66	100	Natural
ETN-1 (Etna)	47.95	1.67	17.32	10.24	0.17	5.76	10.93	3.45	1.99	0.51	100	Natural
PST-9 (Stromboli)	49.82	0.81	15.94	7.71	0.20	8.07	12.81	2.32	1.92	0.40	100	Natural

Measurements are from electron microprobe analysis in oxide wt%, standard deviations are italicized, number of analyses listed in parentheses. Also listed are compositions from Lesne et al. (2011a, b) for comparison

[a]Total iron expressed as FeO

Stromboli (Italy), a trachybasalt from Etna (Italy), a basaltic andesite from the San Francisco Volcanic Field (SFVF, AZ, USA), and phonotephrites from Erebus (Antarctica) and Vesuvius (Italy). These compositions range in total alkali content from ~ 4 to 9 wt%, with variable Na_2O/K_2O ratios and all but the Vesuvius composition containing more Na_2O than K_2O. Notably, the Vesuvius and Erebus compositions have similar total alkali contents and nearly reciprocal Na_2O/K_2O ratios. The other four compositions differ in total alkali content by only 1 wt%. SiO_2 content is between ~ 47.5 and 49 wt% in all but the SFVF composition, which has nearly 53 wt% SiO_2. The compositions exhibit a wide range of MgO (~ 3.3 to 8.7 wt%) and CaO (~ 7 to 12.5 wt%) contents. Smaller variations are found in iron (expressed as FeO; ~ 8 to 11 wt%) and Al_2O_3 (~ 15 to 19 wt%). One motivation for the inclusion of the Stromboli, Etna, and Vesuvius magmas is that Lesne et al. (2011a, b) recently conducted low-pressure volatile solubility experiments on these compositions. Additional experiments on these compositions at mid-crustal pressures can yield valuable insight into the accuracy of extrapolating solubility models. Furthermore, incorporation of the lower pressure results from Lesne et al. (2011a, b) with the new experimental data at higher pressure from this study will permit modeling of volatile solubility over a larger compositional and pressure range.

All experimental work and sample preparation were conducted in the high-pressure facility at Arizona State University (ASU). Three natural samples were collected, and the remaining three compositions were synthesized from powdered oxide and carbonate components to match specific magma compositions from the literature (Table 1). Starting glasses were dried and homogenized or synthesized from oxide powders. For the natural samples, a small amount of material (~ 5 g) was first broken up into coarse pieces using carbide anvils with a Carver press, and then finely crushed under ethanol using an agate mortar and pestle. This rock was placed in an iron-saturated Pt crucible, heated in a 1 atm gas-mixing furnace set to 1400 °C at fO_2 conditions equal to the NNO buffer controlled by a $CO–CO_2$ gas mixture for at least 90 min, and then drop-quenched into water. For the synthesized samples, approximately 4 g total of powdered oxides was measured out based on the components of the published compositions and then mixed together under ethanol using an agate mortar and pestle. The powdered mixture was melted using the same gas-mixing furnace conditions as for the natural samples for just 30 min. The synthesized glass was removed, crushed, and sent through another 30-min cycle in the gas-mixing furnace to ensure homogeneity. The resulting glasses were verified to reproduce the desired compositions by electron microprobe analysis prior to use in experiments.

Experimental setup

Experimental capsules were manufactured from 5 mm-diameter $Au_{80}Pd_{20}$ tubing with lids cut from foil or unwrapped tubing and shaped with a die. Typical capsule lengths were around 5 mm, and exact capsule measurements are recorded in Table 2. The capsules were welded using a 60 W Nd:YAG laser (LaserStar). After attaching one lid, the capsules were filled with approximately 50 mg of dried, crushed starting glass. H_2O and CO_2 were added as oxalic acid dihydrate crystals (1.3–2.6 mg; typically > 2 mg) with additional liquid water (0.25–2.5 mg) added by micro-syringe. The volatile mixture varied based on the exact capsule length and corresponding mass of glass added, approximate expected solubility, and the planned run pressure, targeting primarily CO_2-rich fluid conditions. The masses of components added to the capsules can be found in Table 2. The capsules were sealed and weighed, then placed in a drying oven and later weighed again to check for any leaks prior to use in an experiment.

The solid-media assembly constructed for the piston–cylinder experiments was modified from the NaCl–Pyrex–MgO assembly described in Moore et al. (2008), as shown in the schematic cross section in Fig. 3a. One primary difference is that a small diameter graphite furnace (7.62 mm O.D.) was used to facilitate fast quench rates, and the resulting gap between the Pyrex furnace insulator and outer NaCl was filled with a sleeve made from crushable MgO. A boron nitride (BN) disk was placed above the Pyrex at the top of the capsule to accommodate volume changes within the capsule. The Pyrex furnace insulator was spiral cut to facilitate even compression of the assembly during pressurization and minimize potential deformation of the graphite furnace. Note that one experiment, SU-1, was run using the larger diameter furnace (10.85 mm O.D.) designed for the 19-mm assembly. Experiments SU-1 and SU-2 did not include a BN disk at the top of the capsule in their assemblies. The capsules in experiments Z-15 and Z-22 were packed with Pyrex powder inside a BN capsule. The BN capsule approach was not pursued further because smooth and symmetric deformation of the brittle $Au_{80}Pd_{20}$ capsule was best achieved in the assembly design shown in Fig. 3a.

Experiments

Volatile solubility experiments were conducted in a non-end-loaded piston–cylinder apparatus. The pressure plate was treated with white Molykote HP-300 grease before insertion of the assembly. Each experiment was performed at 1200 °C as recorded by a crossed wire (W5Re–W26Re) thermocouple at the capsule base and a constant pressure between 400 and 600 MPa (see Table 2). These values of pressure were converted from measurements of oil pressure

Table 2 Experimental conditions and results

Experiment	Composition	Added to capsule			Pressure[b] (MPa)	Run time (h)	%FeO kept[c]	In fluid		Weighed fluid loss (mg)	$X^f_{H_2O}$	f_{H_2O} (MPa)	f_{CO_2} (MPa)	In glass[d]	
		Rock (mg)	H_2O (mg)	OAD (mg)[a]				H_2O (mg)	CO_2 (mg)					H_2O (wt%)	CO_2 (ppm)
SU-7	SFVF	45.15	2.58	1.31	413.3	24.33	96.16	n/a	0.779	1.06	0.441*	208	598	5.27	2040
SU-1	SFVF	55.69	1.30	2.34	425.5	22.90	95.74	0.083	1.569	1.73	0.115	50	1021	2.39	3049
SU-6	SFVF	51.41	2.39	2.03	612.3	26.58	97.48	n/a	1.223	1.39	0.213*	173	2026	4.77	4963
SU-2	SFVF	43.73	1.80	2.30	614.1	22.40	94.42	0.104	1.473	1.63	0.148	108	2251	3.90	5520
Z-32	Sunset	56.86	1.25	2.44	407.1	24.00	90.00	0.153	1.648	1.84	0.185	85	845	2.61	3176
SB-3	Sunset	51.92	1.53	2.23	518.0	22.98	88.66	0.098	1.415	1.50	0.145	92	1490	3.32	4535
SB-4	Sunset	55.87	1.82	2.34	609.8	23.05	87.18	0.142	1.358	1.57	0.204	165	2029	4.12	6086
Z-31	Erebus	58.84	1.40	2.19	407.8	18.50	86.10	n/a	1.673	1.80	0.112*	52	924	2.52	3368
EB-4	Erebus	55.07	0.57	2.37	524.7	23.00	79.87	0.073	1.535	1.61	0.105	68	1606	2.32	5386
EB-5	Erebus	50.38	0.26	2.41	617.5	22.30	75.80	0.038	1.530	1.63	0.058	48	2476	2.12	6754
VS-1	Vesuvius	46.13	1.23	2.25	412.7	22.72	85.96	n/a	1.457	1.68	0.229*	107	823	3.43	4963
VS-3	Vesuvius	48.42	0.51	2.69	519.8	22.52	83.46	0.084	1.564	1.75	0.116	74	1552	2.74	6845
Z-33	Vesuvius	58.73	2.25	2.69	607.7	23.97	86.91	0.088	1.513	1.69	0.125	100	2213	3.95	8501
VS-2	Vesuvius	46.45	1.86	2.49	622.1	24.00	87.28	n/a	1.397	1.45	0.023*	19	2614	4.62	9542
ET-8	Etna	43.02	1.18	2.15	404.1	23.97	83.15	n/a	1.481	1.70	0.222*	101	795	2.68	3996
Z-22	Etna	102.04	2.60	3.52	419.4	23.07	81.40	0.249	2.309	2.62	0.209	100	872	3.35	4426
ET-9	Etna	50.72	1.50	2.21	518.3	22.33	85.52	0.176	1.425	1.62	0.232	148	1340	4.24	5395
ET-5	Etna	45.45	1.83	2.24	616.8	24.03	82.57	n/a	1.361	1.60	0.259*	213	1943	5.19	7072
Z-15	Etna	42.92	1.73	2.25	619.9	21.02	81.59	0.127	1.411	2.02^	0.180	149	2175	4.53	7659
ST-3	Stromboli	50.75	1.13	2.17	427.0	22.58	80.59	0.115	1.428	1.59	0.164	81	957	2.33	3568
ST-6	Stromboli	53.84	1.52	2.22	519.2	22.67	85.15	0.025	1.303	1.35	0.044	28	1674	2.64	5272
ST-4	Stromboli	50.62	1.91	2.12	608.0	22.97	85.38	0.131	1.203	1.42	0.209	169	2001	4.16	6086

[a]*OAD* oxalic acid dihydrate

[b]Pressure calculated from oil pressure of piston cylinder

[c]Proportion of FeO kept in the glass relative to the initial glass FeO concentration, calculated as $100*FeO_{glass}/FeO_{starting\ glass}$, with $FeO_{starting\ glass}$ from Table 1, with composition analyses normalized to 100% anhydrous and all Fe as FeO

[d]Reported here for quick reference; refer to Table 3 for determination of glass volatile contents

^Capsule retained material from assembly after cleaning in HF, some of which came off during manometry analysis resulting in the poor agreement between fluid measured by manometry and weighed fluid loss

* Fluid composition estimated from weight loss and CO_2 measured from manometry (see supplementary material)

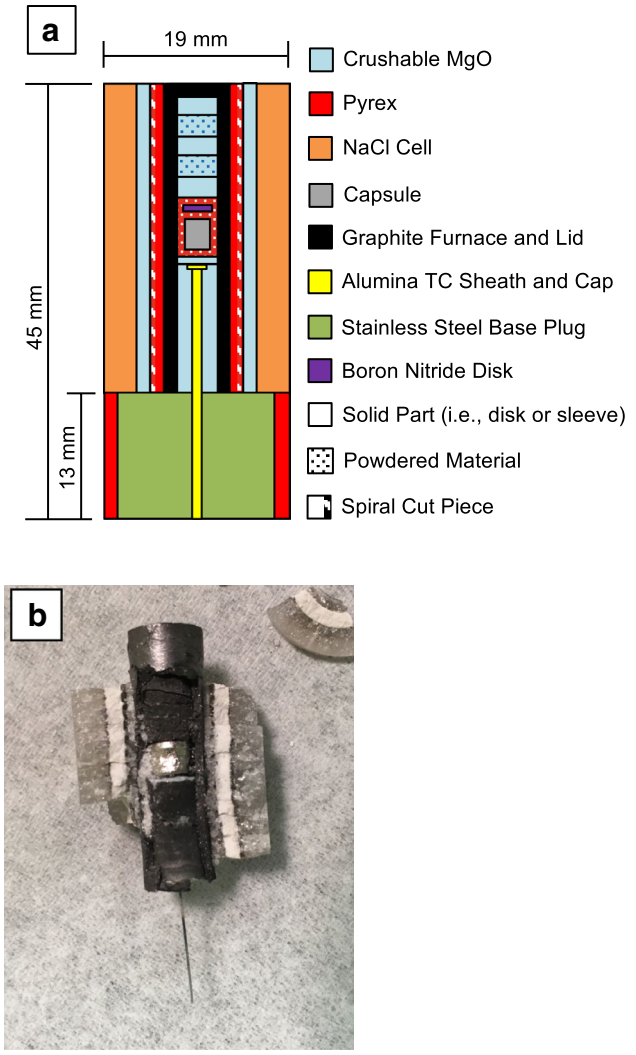

Fig. 3 Experimental assembly. **a** Representative schematic of the experimental assembly in cross section. Note that several experiments used a slightly modified assembly as detailed in the text. **b** Post-run assembly of experiment VS-3. The base plug has been removed where thermocouple lead is exposed, and concentric layers (moving inward) of NaCl, crushable MgO, Pyrex and graphite are visible. The white material in contact with the left side of the deformed experimental capsule is Pyrex, and the material above and below the capsule is crushable MgO that appears black at its outer surface from contact with the graphite furnace

using a Heise gauge. The heating and pressurization routine took place in three stages. The assembly was first pressurized to ~ 100 MPa, then simultaneously heated and pressurized at rates of ~ 30 °C min^{-1} and ~ 25 MPa min^{-1} until the maximum pressure was reached around 500–600 °C. The remaining heating was carried out under isobaric conditions. The experiments were run for approximately 24 h to achieve full homogenization and then quenched isobarically. The quench rate was approximately 85 °C s^{-1} during the initial temperature drop, and while the rate slowed as the quench progressed, all experiments reached 800 °C within 5.5 s and cooled to 350 °C within 16.5 s.

After each run, the assembly was removed, cracked open to retrieve the capsule, and carefully inspected. An example of an opened assembly post-run, after removal of the base plug, is shown in Fig. 3b. The furnace was checked for any fractures, and geometric measurements were taken to confirm that the centered position of the capsule had not changed during compression and heating of the assembly. A fractured furnace could facilitate diffusion of carbon through the assembly, but none of the successful experiments in this study had fractures or irregularities in the furnace upon inspection post-run. Capsules outside of the central "hot spot" of the furnace may experience lateral temperature variations, but none of the experiments in this study had capsule positions outside of the central hot spot. Additionally, the capsules in this study were relatively short (~ 5 mm), which helped to minimize the potential influence of the thermal gradient. After extraction from the assembly, the capsules were cleaned with hydrofluoric acid to remove all Pyrex glass attached to the capsule exterior. Capsules were then weighed and any that registered mass loss during the run were not analyzed.

Analytical techniques

Fluid composition analysis

To calculate solubility relationships from the experiments, the composition of the fluid in equilibrium with the liquid (magma + dissolved volatiles) must be measured. Assuming Henrian behavior in this range of experimental conditions, the dissolved volatile content is proportional to the pressure (fugacity) from the fluid phase. The fluid composition of successful experiments was measured using vacuum manometry. The capsules were punctured under vacuum, and the fluid was frozen in liquid nitrogen and dry ice–ethanol traps to separate the H_2O and CO_2.

Each volatile species was moved to a U-tube manometer using a Toepler pump, and the height of the Hg columns was measured using a cathetometer. H_2O was reduced to hydrogen gas prior to measurement using heated uranium or chromium. The hydrogen reduction failed for several capsules (see Table 2) because the metal catalyst was exhausted. For these capsules, the H_2O in the fluid was calculated by difference (refer to supplementary material). We estimate the error of the CO_2 analysis to be 1%, and for H_2O, 5%. The error in estimated H_2O fluid for the capsules with failed hydrogen reduction may reach 20%.

A non-condensable fluid was also typically present in the capsules, indicated by a non-zero residual pressure. This residual pressure was noted and then the gas was pumped away,

but in rare cases the non-condensable fluid was measured by manometry. Analysis of the non-condensable fluid indicated that it was at micromole abundance in the experiments presented here and likely represents nitrogen from air introduced during capsule filling. Capsules sealed under vacuum for another experimental study, which incorporated less air than the capsules in this study sealed at ambient conditions, had roughly one-third the abundance of a non-condensable fluid phase, consistent with nitrogen from air as the source of this fluid.

Major element analysis

Starting glasses (both natural and synthesized) and glass chips from each experiment were mounted in epoxy, polished, carbon coated, and analyzed for major elements using a Cameca SX100 Ultra electron microprobe at the University of Arizona. Natural crystals and synthetic glasses were used as standards. Each element was counted for 20 s (10 s for Na, counted first in the sequence) using 15 keV accelerating voltage, 20 nA beam current, and a 15 µm spot size. At least four spots spread out across the glass chips were analyzed for each sample. In all cases, the analyses demonstrated homogeneous starting glass compositions.

Dissolved volatile content analysis

H_2O and CO_2 contents of the experiments were determined by Fourier transform infrared spectroscopy (FTIR). Doubly polished wafers of glass chips from each experiment were polished by hand for transmission FTIR analysis. We analyzed a minimum of three wafers of variable thickness (~ 200 µm, ~ 90 µm, and ~ 50 µm) from each experiment to obtain good absorbance peaks for each volatile species. For most experiments, wafers of six different thicknesses (~ 200 µm, ~ 90 µm, ~ 60 µm, ~ 50 µm, ~ 40 µm, and ~ 30 µm) were prepared to account for a wide range of H_2O and CO_2 contents. The CO_2 content was determined from the CO_3^{2-} absorption doublet around 1500 cm^{-1}. The total H_2O was determined from individual water species (OH^- and H_2O_{mol}) in the near-IR range around 4500 cm^{-1} and 5200 cm^{-1}, respectively. FTIR analyses were performed using a Nicolet iN10 MX instrument at the United States Geological Survey in Menlo Park. Spectra were collected between 5500 and 1000 cm^{-1} wavenumber for 45 s (128 scans) with high spectral resolution using a 50 µm × 50 µm aperture, and a background was collected before analyzing each sample.

H_2O and CO_2 contents were calculated using the Beer-Lambert Law

$$C = \frac{\mathrm{MW} * A}{\rho * \varepsilon * d}, \quad (1)$$

where C is the concentration in wt%, MW is the molecular weight of the absorbing species, A is the peak height (absorbance) of interest, d is the sample thickness in cm, ρ is the density of the sample in g L^{-1}, and ε is a molar absorption coefficient in L mol cm^{-1}. Thicknesses were determined using a Zygo ZeScope optical profilometer in the LeRoy Eyring Center for Solid State Science at ASU. For selected samples, interference fringes in the transmission FTIR spectra were used to confirm thicknesses (e.g., Nichols and Wysoczanski 2007). The average difference between thickness measurements from the two techniques was less than 3 µm, consistent with the standard deviation reported in Nichols and Wysoczanski (2007) of the difference in thickness of glass chips measured both by the fringe method and a digital displacement gauge. Glass density was determined for each experiment using the method detailed in Luhr (2001) wherein molecular partial molar volume contributions are totaled for dry glass and density is calculated iteratively based on water content.

Molar absorption coefficients vary by glass composition (e.g., Dixon and Pan 1995; Dixon et al. 1995; Mandeville et al. 2002). These piston–cylinder experiments do not produce enough material for bulk volatile determinations, and so new molar absorption coefficients for these compositions were not calibrated. However, the relationship from Dixon and Pan (1995) that correlated absorption coefficients for CO_2 (dissolved as CO_3^{2-}) to Na–Ca contents of alkali-rich mafic magmas was calibrated using magmas that span the range of compositions in this study. The ε_{CO_2} values (in L mol cm^{-1}) calculated for each composition using the method of Dixon and Pan (1995) for the ~ 1520 cm^{-1} peak are as follows: 314 for Sunset Crater, 309 for SFVF, 235 for Erebus, 369 Vesuvius, 325 for Etna, and 358 for Stromboli. For water species, the most appropriate molar absorption coefficients for this compositional range are 63 L mol cm^{-1} for $\varepsilon_{H_2O^{tot}}$ from Dixon et al. (1988), and for the near-IR peaks, 0.67 L mol cm^{-1} for ε_{OH^-} and 0.62 L mol cm^{-1} for $\varepsilon_{H_2O^{mol}}$ from Dixon et al. (1995).

The measurement of absorbance from an FTIR spectrum and the molar absorption coefficient are inherently linked, because absorption coefficients vary depending on the selected baseline subtraction technique (e.g., Ohlhorst et al. 2001). In Dixon and Pan (1995), absorbance values are measured after subtraction of a spectrum of a volatile-free sample of the same composition, corrected for density and sample thickness. The subtracted spectrum must be an accurate structural match, meaning that the resulting baseline-corrected spectrum from ~ 1275 to 1975 cm^{-1} appears essentially flat with three peaks: one from molecular H_2O (in hydrous samples), and two sub-equal peaks from the carbonate doublet (e.g., Fig. 1b in Dixon et al. 1995). French-curve (flexicurve) baselines were used to reproduce the spectra

of volatile-free samples to match the baseline subtraction techniques that produced the absorption coefficients.

It has been suggested that the Na–Ca relationship of Dixon and Pan (1995) may not be valid for potassium-rich glasses (i.e., the Vesuvius composition). However, the absorption coefficient value determined by Behrens et al. (2009) for an ultra-potassic magma agrees with the Dixon and Pan (1995) trend within error. Other recent studies of natural magmas (e.g., Shishkina et al. 2010, 2014) have also determined new coefficients for alkali-rich magmas that mostly agree with the Dixon and Pan (1995) trend, within error, despite some differences in results from the baseline subtraction.

Calculated volatile contents from FTIR data are optimized in this study in two different ways. First, the optical profilometry utilized to calculate the thickness of each sample produces a thickness map for the entire sample, and so the precise thickness (nm resolution) across the FTIR aperture was easily determined. Second, several wafers for each experiment with variable thicknesses were analyzed to provide multiple independently calculated values for volatile contents, which generally agree within < 100 ppm for CO_2 and < 0.05 wt% for H_2O determined by near-IR peaks. For these reasons, the uncertainty in the dissolved volatile content calculations is primarily related to absorption coefficients and not to the other variables. The corresponding uncertainty in glass CO_2 contents is estimated to be 5% for the Sunset Crater, SFVF, Etna, and Stromboli compositions, which for reference would correspond with ± ~ 15 L mol cm^{-1} error in ε_{CO_2} values. Because the Vesuvius and Erebus compositions are just beyond the calibrated compositional range of the Dixon and Pan (1995) relationship, we estimate higher error in CO_2 glass contents of 10% for these two compositions. Because we do not change molar absorption coefficients for H_2O by magma composition, we estimate 10% error in all H_2O glass measurements.

Results

The experiments conducted in this study were designed to quantify and describe CO_2 solubility in alkali-rich mafic magmas at mid-crustal pressures. Mixed (H_2O–CO_2) fluid rather than pure CO_2 experiments were conducted for several reasons. First, there is a possibility of reduced CO_2 solubility at very low water contents (e.g., Ghiorso and Gualda 2015), and so these experiments constrain CO_2 solubility in the presence of H_2O. Most natural magmas have mixed fluid compositions (e.g., Métrich et al. 2010; Hartley et al. 2014; Allison 2018; Moore et al. 2015; Aster et al. 2016) and these experiments therefore replicate conditions within the natural magmatic system. Additionally, use of mixed fluid compositions yields greater flexibility in the CO_2 fugacity. To obtain data at high CO_2 fugacities (and therefore higher CO_2 partial pressures) in these mixed experiments, CO_2-rich fluid compositions were targeted. This was achieved by adding only small amounts of liquid water in addition to the oxalic acid dihydrate crystals to the capsules as sources of volatiles. Accordingly, we first explain results from the fluid composition analysis and the calculated fugacities (f_{CO_2} and f_{H_2O}) for each volatile species. We continue with details of the oxygen fugacity conditions of the experiments and observations of the experimental glasses. The volatile solubility of each composition is then described by the trend between fugacity and dissolved volatile contents.

Manometry and fugacity

Analyses of capsule fluids are summarized in Table 2. The manometry analysis indicated that nearly all of the fluid in the capsule was represented by H_2O and CO_2. In experiments for which both H_2O and CO_2 were measured by manometry (15 experiments), the fluid mass determined by manometry represented on average 96% of the total mass lost from the capsule upon puncture. Excluding experiment Z-15 from this average, which lost some non-fluid mass during puncture in the form of assembly material stuck to the capsule, improves this average to 98%. Non-condensable fluids, primarily nitrogen from air incorporated in the capsule, therefore represent only a very small mass fraction of the fluid. With one exception, all the experiments were run at CO_2-rich conditions, with fluid compositions < 0.26 mole fraction H_2O ($X^f_{H_2O}$). The more water-rich fluid in experiment SU-7 achieved lower CO_2 fugacity while still running within our defined pressure range. The Erebus experiments were specifically run at very CO_2-rich conditions to keep water contents (and therefore total volatile contents) low to avoid FTIR spectra with merged carbonate peaks (see Iacovino et al. 2013). On average, the $X^f_{H_2O}$ in this study is 0.170.

The pure H_2O and CO_2 fugacities for each experiment were calculated using the modified Redlich–Kwong equation of state (Holloway 1981; 1987; Holloway and Blank 1994) with the Saxena and Fei (1987) high-pressure correction. MATLAB codes to calculate fugacities, translated from Quickbasic scripts given in Holloway and Blank (1994), are included in the supplementary material. Additionally, an Excel spreadsheet provided in the supplementary material includes options to calculate fugacity and partial pressures of H_2O and CO_2 using the fugacity model from Holloway and Blank (1994). The specific H_2O and CO_2 fugacities of each experiment, listed in Table 2, are calculated from the pure fluid fugacity of each species multiplied by the fluid mole fraction of the species.

Oxygen fugacity

The oxygen fugacity (f_{O_2}) conditions were not varied during these experiments. Some experimental studies in internally heated pressure vessels have noted a direct correlation between experimental f_{O_2} and capsule fluid composition ($X^f_{H_2O}$; e.g., Botcharnikov et al. 2005b). In those experiments, capsules with H_2O-poor fluids, like the ones in this study, would have a tendency to gain hydrogen through diffusion, thereby creating reducing conditions in the capsule (Botcharnikov et al. 2005b). This relationship suggests that variation in fluid composition from high to low $X^f_{H_2O}$ would result in more than several log units change in f_{O_2}. While this concern is valid for experiments in gas vessels, the experimental setup described here was designed specifically to avoid changing f_{O_2} conditions from hydrogen diffusion.

The oxygen fugacity was not directly measured during these new experiments, but there are several lines of evidence to indicate oxidizing conditions for all experiments. First, the intrinsic f_{O_2} of the piston–cylinder used in this study is NNO + 1 (Iacovino et al. 2013). Second, the solid-media components of the assembly were chosen to prevent diffusion and the crushable MgO used throughout the assembly is irreducible, which acts to buffer f_{O_2} to oxidizing conditions. Third, several similar experiments using an oxygen sensor were conducted and indicate that oxidizing conditions are maintained at low $X^f_{H_2O}$. The sensor consisted of nickel and nickel oxide powder sealed in a 2 mm Pt capsule, which was placed inside the $Au_{80}Pd_{20}$ experimental capsule. Small additions of oxalic acid dihydrate provided H_2O, with the capsules sealed under vacuum to set $X^f_{H_2O} < 0.1$, but other details of the assembly were identical to those used in this study. Post-run analysis showed that the sensor capsules contained only nickel oxide, consistent with oxidizing conditions above NNO even at low $X^f_{H_2O}$.

Finally, results of fluid manometry are also consistent with high experimental f_{O_2}. There is no evidence that reduced volatile phases such as CO and CH_4 are present in capsule fluids. If CO or CH_4 were present, they would not condense at liquid nitrogen temperatures at vacuum pressure and would contribute to significant non-condensed fluid. Additionally, if f_{O_2} was decreasing with $X^f_{H_2O}$, there would be a correlation between the amount of non-condensed fluid and $X^f_{H_2O}$. Instead, the amount of non-condensed fluid is uniformly low (micromole level) and shows no correlation with $X^f_{H_2O}$. In fact, as described in "Fluid composition analysis", the results of a separate study show that the non-condensed fluid in vacuum-sealed capsules, with very CO_2-rich fluid (i.e., $X^f_{H_2O} < 0.1$), is roughly one-third of that of capsules sealed in air. This observation is consistent with the non-condensed phase being composed of nitrogen. This evidence, combined with the excellent mass balance of manometry measurements, indicates that only H_2O, CO_2, and a negligible amount of nitrogen are present in the capsule fluids. This result confirms that the experimental capsules essentially contain a pure mixed fluid of H_2O and CO_2.

Physical observations and major element composition

Quenched run products from successful experiments range in color from brownish to black glass. Glasses from Erebus experiments are nearly opaque in thicker chips, possibly due to high Ti content (Iacovino et al., 2013), but still exhibit vitreous luster overall and appear translucent in thinner samples. Quench microcrystals are very rare and do not make up any significant portion of the glass. Rare plagioclase microphenocrysts were only observed in glasses from experiments SU-2 and SU-7. Imprints of bubbles can be observed at the top of the capsules, providing additional proof of fluid saturation at run conditions. Glass chips selected for analysis were not taken from the very top portion of the capsule to avoid any micro-bubbles or crystals that could be present.

Experiment glasses exhibit homogeneity in their major element compositions with some iron loss to the capsule. As shown in Table 2, approximately 86.5% of the iron was retained from the starting composition. Full major element compositional data for each experiment is provided in the supplementary material. With the exception of some Fe loss, all other elements show good agreement with the composition of the starting glass. Calculated glass densities are between ~ 2550 and 2700 g L^{-1} (Table 3).

Carbon dioxide

Results of the infrared analysis of CO_2 contents of experimental glasses are plotted in Fig. 4 and listed in Tables 2, 3. The CO_2 contents of each experiment are reproducible within ~ 100 ppm from multiple wafers of variable thicknesses. For ease of comparison, the compositions with lower CO_2 solubilities, Sunset Crater, SFVF, and Erebus, are shown in Fig. 4a and the remaining compositions are shown in Fig. 4b. In Fig. 4a, best fit curves using power law fits are plotted through the Sunset Crater and SFVF experiments to compare the relative solubility differences between these two compositions.

CO_2 contents for experiments on the Stromboli, Etna, and Vesuvius compositions are shown in Fig. 4b. We have included CO_2 data at low pressures from Lesne et al. (2011b) as circles in Fig. 4b, and these values have been adjusted to utilize the Dixon and Pan (1995) absorption coefficients for carbonate for uniform comparison with our data. Accordingly, we also adjust the fugacity values of the Lesne et al. (2011b) data as they differ slightly from values

Table 3 FTIR data for experiments

Composition	Experiment	Wafer	Thickness (cm)	Density (g L^{-1})	A_{5200}	A_{4500}	A_{3500}	$A_{\sim1510}$	H_2O wt% (total, NIR)[a]		H_2O wt% (3500)[b]	CO_2 (ppm)[c]	
SFVF	SU-7	1	0.0228	2548	0.0594	0.0497			**5.27**	*0.02* (*6*)			
SFVF	SU-7	3	0.0077	2548	0.0186	0.0183		0.281	5.26			**2040**	*17* (*5*)
SFVF	SU-1	a1	0.0219	2631	0.0161	0.0339			**2.39**	*0.02* (*7*)			
SFVF	SU-1	b3	0.0098	2631	0.0071	0.0152	1.638	0.552	2.39		1.82	**3049**	*60* (*6*)
SFVF	SU-6	1	0.0192	2567	0.0428	0.0411			**4.77**	*0.02* (*4*)			
SFVF	SU-6	4	0.0054	2567	0.0115	0.0121	1.633	0.483	4.76		3.37	**4963**	*56* (*4*)
SFVF	SU-2	a1	0.0203	2585	0.0314	0.0421			**3.90**	*0.03* (*8*)			
SFVF	SU-2	c2	0.0056	2585	0.0084	0.0119	1.482	0.561	3.90		2.93	**5520**	*106* (*4*)
Sunset	Z-32	1	0.0187	2719	0.0133	0.0350		1.114	**2.61**	*0.01* (*4*)		3071	
Sunset	Z-32	3	0.0068	2719	0.0053	0.0124	1.454	0.419	2.64		2.25	**3176**	*56* (*5*)
Sunset	SB-3	1	0.0211	2695	0.0274	0.0405			**3.32**	*0.01* (*6*)			
Sunset	SB-3	4	0.0057	2695	0.0109	0.0076	1.573	0.497	3.39		2.93	**4535**	*63* (*5*)
Sunset	SB-4	1	0.0203	2670	0.0298	0.0509			**4.12**	*0.01* (*6*)			
Sunset	SB-4	6	0.0037	2670	0.0060	0.0086	1.120	0.429	4.11		3.24	**6086**	*67* (*5*)
Erebus	Z-31	2	0.0104	2626	0.0075	0.0175		0.494	**2.52**	*0.05* (*6*)		3388	
Erebus	Z-31	3n	0.0054	2626	0.0015	0.0118	1.277	0.255	2.55		2.58	**3368**	*67* (*8*)
Erebus	EB-4	1	0.0193	2623	0.0114	0.0314			**2.32**	*0.03* (*5*)			
Erebus	EB-4	5	0.0046	2623	0.0029	0.0074	0.911	0.347	2.35		2.16	**5386**	*60* (*5*)
Erebus	EB-5	1	0.0236	2621	0.0136	0.0341			**2.12**	*0.02* (*5*)			
Erebus	EB-5	4	0.0053	2621	0.0024	0.0084	0.905	0.501	2.13		1.86	**6754**	*16* (*4*)
Vesuvius	VS-1	1	0.0212	2639	0.0250	0.0444			**3.43**	*0.02* (*6*)			
Vesuvius	VS-1	4	0.0053	2639	0.0062	0.0110	1.218	0.582	3.40		2.49	**4963**	*53* (*5*)
Vesuvius	VS-3	1	0.0191	2658	0.0149	0.0357			**2.74**	*0.03* (*5*)			
Vesuvius	VS-3	4	0.0059	2658	0.0044	0.0113	1.114	0.900	2.75		2.03	**6845**	*21* (*5*)
Vesuvius	Z-33	1	0.0201	2626	0.0358	0.0388			**3.95**	*0.01* (*5*)			
Vesuvius	Z-33	5	0.0046	2626	0.0081	0.0090	1.451	0.861	3.95		3.44	**8501**	*93* (*4*)
Vesuvius	VS-2	1	0.0193	2604	0.0454	0.0373			**4.62**	*0.03* (*6*)			
Vesuvius	VS-2	6	0.0042	2604	0.0088	0.0091	1.391	0.875	4.58		3.64	**9542**	*40* (*3*)
Etna	ET-8	1	0.0203	2683	0.0145	0.0386			**2.68**	*0.02* (*5*)			
Etna	ET-8	4	0.0061	2683	0.0045	0.0114	1.248	0.483	2.67		2.18	**3996**	*37* (*5*)
Etna	Z-22	3	0.0148	2666	0.0149	0.0331		1.233	**3.35**	*0.02* (*4*)		4232	
Etna	Z-22	6	0.0084	2666	0.0092	0.0176		0.732	3.31			**4426**	*180* (*4*)
Etna	ET-9	1	0.0208	2640	0.0303	0.0539			**4.24**	*0.02* (*4*)			
Etna	ET-9	4	0.0058	2640	0.0088	0.0147	1.530	0.610	4.25		2.86	**5395**	*53* (*5*)
Etna	ET-5	1	0.0208	2607	0.0497	0.0509			**5.19**	*0.03* (*6*)			
Etna	ET-5	5	0.0039	2607	0.0092	0.0097	1.427	0.531	5.20		4.01	**7072**	*50* (*3*)

Table 3 (continued)

Composition	Experiment	Wafer	Thickness (cm)	Density (g L^{-1})	A_{5200}	A_{4500}	A_{3500}	$A_{\sim1510}$	H_2O wt% (total, NIR)[a]		H_2O wt% (3500)[b]	CO_2 (ppm)[c]	
Etna	Z-15	4	0.0050	2624	0.0112	0.0100	1.560	0.740	**4.53**	*0.04* (2)	3.40	7638	
Etna	Z-15	5	0.0038	2624	0.0081	0.0081	1.327	0.564	4.55		3.81	**7659**	*48* (3)
Stromboli	ST-3	1	0.0194	2680	0.0137	0.0303			**2.33**	*0.03* (6)			
Stromboli	ST-3	4	0.0068	2680	0.0044	0.0113	1.400	0.529	2.37		2.20	**3568**	*30* (6)
Stromboli	ST-6	1	0.0210	2676	0.0184	0.0353			**2.64**	*0.02* (6)			
Stromboli	ST-6	4-2	0.0042	2676	0.0036	0.0072	1.017	0.482	2.65		2.59	**5272**	*18* (6)
Stromboli	ST-4	1	0.0187	2634	0.0284	0.0455			**4.16**	*0.02* (5)			
Stromboli	ST-4	5	0.0049	2634	0.0070	0.0121	1.311	0.639	4.10		2.91	**6086**	*86* (6)

Accepted volatile concentrations for each experiment are listed in bold type with the standard deviation of the average concentration in italics for the number of samples in parentheses

[a] H_2O content calculated from near-IR FTIR data using ε coefficients (in l mol^{-1} cm^{-1}) of 0.67 for ε_{OH^-} and 0.62 for $\varepsilon_{H_2O^{mol}}$ from Dixon et al. (1995)

[b] H_2O content calculated from mid-IR FTIR data using an ε coefficient (in l mol^{-1} cm^{-1}) of 63 for $\varepsilon_{H_2O^{tot}}$ from Dixon et al. (1988)

[c] ε_{CO_2} values (in l mol^{-1} cm^{-1}) used for calculating CO_2 contents from the carbonate doublet were calculated for each composition using the method of Dixon and Pan (1995) and are as follows: 314 for Sunset Crater, 309 for SFVF, 235 for Erebus, 369 Vesuvius, 325 for Etna, and 358 for Stromboli

calculated from the modified Redlich–Kwong equation of state that is used in this study. The power curve (dotted) for the Sunset Crater composition is also plotted in Fig. 4b for comparison with these other compositions. The dashed lines in Fig. 4b represent power law fits from Lesne et al. (2011b) that have been extrapolated for comparison with our high-pressure data and will be discussed later.

The lowest CO_2 solubility is recorded by the most evolved composition, the basaltic andesite (SFVF). It is also notable that three of the other experimental compositions show CO_2 solubility relationships that are indistinguishable from each other. The Sunset Crater and Stromboli alkali basalts, as well as the Erebus phonotephrite, show trends of CO_2 concentration versus fugacity that largely overlap. The highest CO_2 solubilities are recorded by two of the three compositions with high total alkali contents. The Etna trachybasalt and the Vesuvius phonotephrite record the highest CO_2 solubilities, with the Vesuvius composition dissolving the most CO_2 of all six compositions in this pressure range.

To estimate overall CO_2 solubility in this pressure range, we use power law fits through the experimental data. We calculate new power law regressions for these compositions using the Lesne et al. (2011b) low-pressure data in addition to our new experiments and yield the following equations, where f_{CO_2} is the CO_2 fugacity:

$$CO_2(\text{ppm}) = 1.050 * f_{CO_2}^{1200^\circ C\ 0.883}; \quad R^2 = 0.996 \text{ for Stromboli,} \tag{2}$$

$$CO_2(\text{ppm}) = 2.831 * f_{CO_2}^{1200^\circ C\ 0.797}; \quad R^2 = 0.990 \text{ for Etna,} \tag{3}$$

$$CO_2(\text{ppm}) = 4.796 * f_{CO_2}^{1200^\circ C\ 0.754}; \quad R^2 = 0.995 \text{ for Vesuvius.} \tag{4}$$

We also calculate power law regressions for the other three compositions in this study, yielding the following equations:

$$CO_2(\text{ppm}) = 3.273 * f_{CO_2}^{1200^\circ C\ 0.740}; \quad R^2 = 0.999 \text{ for SFVF,} \tag{5}$$

$$CO_2(\text{ppm}) = 4.320 * f_{CO_2}^{1200^\circ C\ 0.728}; \quad R^2 = 0.987 \text{ for Sunset Crater,} \tag{6}$$

$$CO_2(\text{ppm}) = 5.145 * f_{CO_2}^{1200^\circ C\ 0.713}; \quad R^2 = 0.983 \text{ for Erebus.} \tag{7}$$

These trends confirm the validity of the assumption of Henrian behavior for CO_2 at these experimental conditions. We note that without lower-pressure data for the SFVF, Sunset Crater, and Erebus compositions, the power law fits may not accurately represent CO_2 solubility at pressures lower than our experimental range.

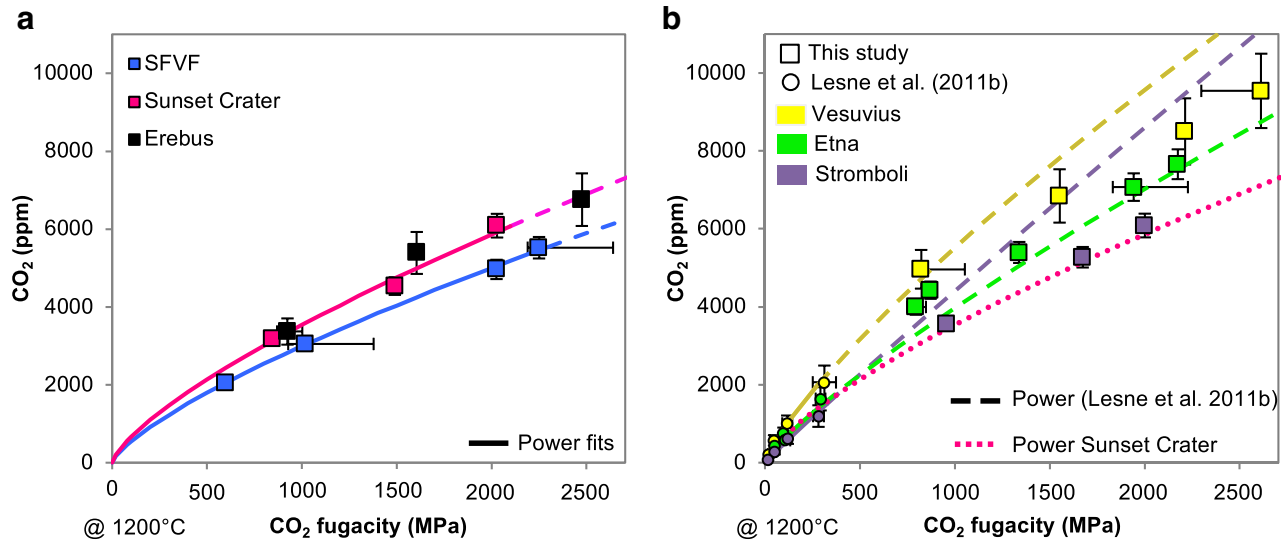

Fig. 4 Dissolved CO_2 concentration versus experiment CO_2 fugacity (squares). **a** Results for the SFVF, Sunset Crater, and Erebus compositions. Curves are power fits through the data for Sunset Crater and SFVF compositions. **b** Results for the Vesuvius, Etna, and Stromboli compositions, including experimental data from Lesne et al. (2011b) shown as circles. Curves are power fits from Lesne et al. (2011b), extrapolated as dashed curves. Power fit from Sunset Crater from Fig. 4a shown as dotted curve for reference

Water

Water contents of these experiments determined from peaks in the near-IR FTIR spectra are between ~ 2.1 and 5.3 wt% across a fugacity range of ~ 20 to 215 MPa (Fig. 5; Tables 2, 3). The water contents of each experiment determined by near-IR peaks are reproducible within ~ 0.05 wt% from multiple wafers of variable thicknesses. Water contents determined by the ~ 3500 cm^{-1} peak sometimes show moderate agreement with the near-IR data, but usually produce lower values (Table 3). The absorbance values for the ~ 3500 cm^{-1} peak are usually > 1, even in many of the thinnest wafers, at which point the height of the peak may not be proportional to concentration (Schrader 1995; von Aulock et al. 2014). These high absorbance values explain why water content calculated from the ~ 3500 cm^{-1} peak is consistently lower than the water content calculated from near-IR peaks, and accordingly why we prefer water contents calculated by near-IR peaks. The overall trends of water content versus fugacity for each composition, shown in Fig. 5 with a power fit for the Etna composition from Lesne et al. (2011a), are generally indistinguishable from each other in this dataset. Experiment VS-2 is the primary exception to the overall trend, likely due to error in its recorded fugacity rather than its measured water content. This experiment had an incomplete fluid measurement by manometry (see "Fluid composition analysis"), which may exaggerate error in the H_2O fugacity.

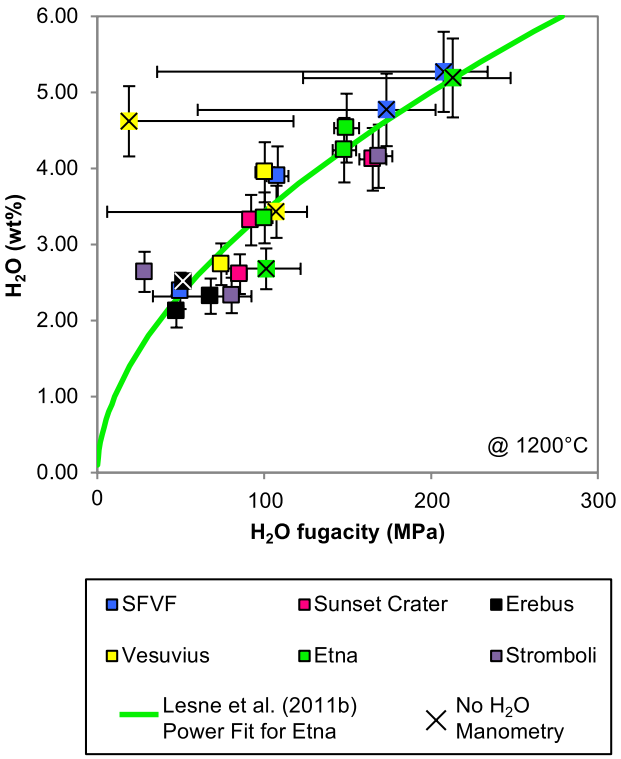

Fig. 5 Dissolved H_2O concentration versus experiment fugacity (squares). Symbols with an *x* represent experiments for which the H_2O manometry failed (see "Fluid composition analysis"). The power law fit for the Etna composition (Eq. 8) from Lesne et al. (2011a) is also included

Discussion

Do existing solubility models describe new experimental data?

We compare our CO_2 solubility data to several existing CO_2 solubility models for alkali-rich mafic magmas as well as to MagmaSat (Ghiorso and Gualda 2015), a mixed H_2O–CO_2 solubility model for all natural magmas. A comprehensive comparison of solubility models is beyond the scope of this work, but these comparisons are included to illustrate how the new experimental data contributes new information to existing understanding of CO_2 solubility. Although it was not the primary objective of this study, we also include a brief comparison of the H_2O solubility data to one of the latest H_2O models for these magma compositions.

Dixon (1997): the *Π* model

The *Π* model of Dixon (1997) was one of the first to constrain CO_2 solubility for a range of alkali-rich mafic magmas. In this approach, major element cation fractions from four mafic compositions were combined into a parameter called *Π*, which was then linearly correlated with CO_2 solubility at constant pressure (1000 bar). While applying this model to natural samples, Dixon (1997) found that *Π* varied linearly with SiO_2 content in glasses from an alkalic ocean island suite, and so SiO_2 content was used as a proxy for *Π*. This parameterization was then integrated into a thermodynamic model (Fine and Stolper 1986; Stolper and Holloway 1988; Dixon et al. 1995) to calculate CO_2 solubility. The thermodynamic model requires at least two empirically determined input parameters (see next section), and one of these parameters was defined using the compositional relationship *Π* (or SiO_2). The other parameter was estimated as a constant for all mafic magmas. The simplified SiO_2-based algorithm of Dixon (1997) was later incorporated into the VolatileCalc H_2O–CO_2 solution model (Newman and Lowenstern 2002), and the *Π* parameterization was included in the SolEx COHSCl volatile solubility model (Witham et al. 2012).

In Fig. 6, we compare the *Π* model to our new experiments. We plot *Π* and CO_2 solubility (as determined by power law fits, Eqs. 2–7) for our six compositions at a pressure of 500 MPa, which is the average pressure in our study. In Dixon (1997), *Π* values are calculated using cation fractions, including Fe^{2+} after correcting iron contents for oxygen fugacity. Therefore, for appropriate comparison with the compositions from Dixon (1997), *Π* values for the six compositions in this study are calculated for an

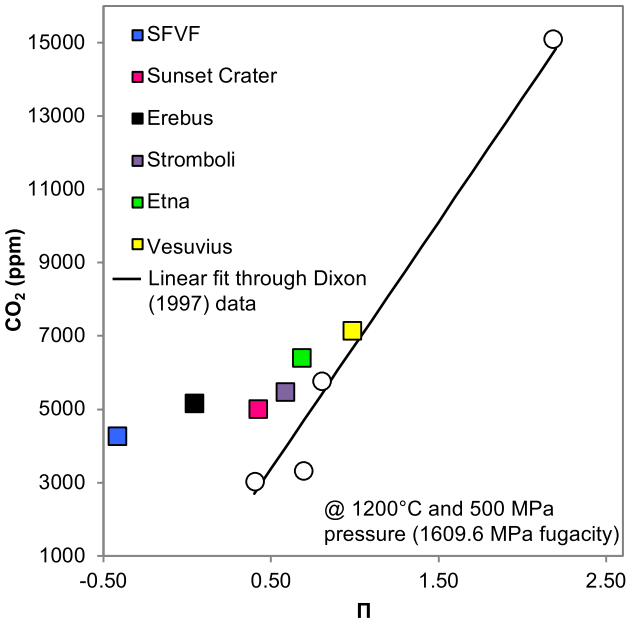

Fig. 6 Comparison of solubility for the six compositions in this study (squares) at 500 MPa to *Π* parameter (Dixon 1997). CO_2 concentrations at 500 MPa are calculated by power law fits through the experimental data (Eqs. 2–7) and *Π* values are calculated assuming an oxidation state corresponding to NNO + 1 as calculated using Kilinc et al. (1983). Also plotted are the *Π* values and CO_2 concentrations at 500 MPa for the four compositions discussed in Dixon (1997), shown as circles, with a linear fit through these data

oxygen fugacity of NNO +1 using the method of Kilinc et al. (1983). Also included in Fig. 6 are the CO_2 solubilities at 500 MPa pressure for the four compositions used in Dixon (1997) to define *Π*. The CO_2 concentrations for these additional compositions were calculated at 500 MPa from the thermodynamic model using the parameters calculated for each composition in the original experimental papers (Pan et al. 1991; Thibault and Holloway 1994; Holloway and Blank 1994; Dixon and Pan 1995; Dixon et al. 1995). The *Π* values of these four compositions are the values given in Dixon (1997). Because *Π* was designed to correlate linearly with CO_2 solubility at constant pressures, a linear regression with a y-intercept of zero is also fit through the Dixon (1997) compositions for reference.

The *Π* model does not perform well for our data. Although Vesuvius appears to fall along the original trend, the mismatch for other compositions becomes progressively worse with decreasing values of *Π*. Overall, the compositions do not follow the simple linear relationship between *Π* and CO_2 solubility that Dixon (1997) observed. Additionally, the three compositions from Dixon (1997) with *Π* values between ~ 0.4 and 1.0 have significantly lower solubilities than the compositions from this study despite nearly identical *Π* values. This discrepancy suggests that there are solubility differences between magmas with similar *Π*

values. We speculate that there may be interactions between components that are not accounted for by the Π parameter. Finally, the Π model cannot calculate CO_2 solubilities for compositions with negative values of Π (Moore 2008), such as the SFVF composition.

Lesne et al. (2011b): empirical power law models

The Lesne et al. (2011b) study contains multiple models, including empirical power law fits as previously mentioned (Fig. 4b). When extrapolated to higher pressure, these power law models overestimate CO_2 solubility in the Vesuvius and Stromboli compositions (Fig. 4b), but show good agreement with the new Etna experiments. We emphasize that Lesne et al. (2011b) do not recommend and did not intend these fits to be used at pressures beyond their experimental range. However, it is still interesting to note that at these higher pressures, the extrapolated Etna and Stromboli low-pressure power fits cross each other (Fig. 4b) and diverge considerably. If these extrapolated fits represent true solubility curves, then we would conclude that CO_2 is much more soluble in the Stromboli magma than in the Etna magma at high pressures (> 500 MPa CO_2 fugacity or ~ 270 MPa pressure for a pure CO_2 fluid) despite the opposite trend at low pressures. Our experimental data do not show any evidence for significant changes in relative CO_2 solubilities between compositions at different pressures, and thus we find it unlikely to occur in natural magmas.

Lesne et al. (2011b): thermodynamic models

The Lesne et al. (2011b) study also includes a thermodynamic approach based on the model of Fine and Stolper (1986), Stolper and Holloway (1988), and Dixon et al. (1995) (described in further detail in the next section). The calculated fits from Lesne et al. (2011b) for each of the three compositions (Vesuvius, Etna, and Stromboli) using the thermodynamic model are plotted with our high-pressure experiments in Fig. 7. When these Lesne et al. (2011b) thermodynamic fits are extrapolated to higher pressures, they show lower CO_2 solubility in the Vesuvius and Etna compositions, and higher CO_2 solubility for Stromboli than what our experiments indicate. As is seen in the extrapolated power law fits, these extrapolated thermodynamic fits also cross and diverge significantly at higher pressures, which suggests that the fits are not realistic above ~ 250 MPa.

Lesne et al. (2011b) also revised the Dixon (1997) general thermodynamic model for mafic magmas, incorporating the low-pressure data on the Stromboli, Etna, and Vesuvius compositions. As was the case in Dixon (1997), the general model presented by Lesne et al. (2011b) uses a compositional relationship for one of the two required thermodynamic parameters, but estimates the other as a constant. This limitation introduces additional uncertainty into the resulting solubility curves.

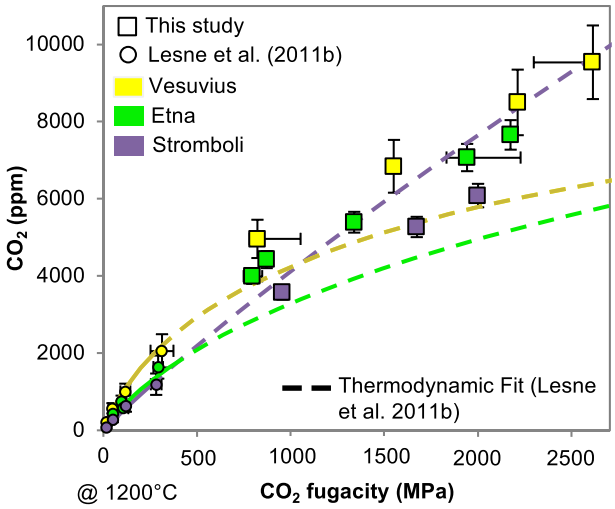

Fig. 7 Dissolved CO_2 concentration versus experimental CO_2 fugacity (squares). The curves were calculated using the thermodynamic models for each composition from Lesne et al. (2011b) (extrapolated as dashed lines). Experiments from Lesne et al. (2011b) are also shown as circles

Other empirical and semi-empirical models

Other models utilize a purely empirical approach. For example, Shishkina et al. (2014) conducted experiments across eight different mafic compositions and produced an exponential relationship between CO_2 content and an updated Π parameterization, again calculated from cation fractions, termed Π*. Figure 8 compares our experimental data, as well as data from the compositions used in Dixon (1997), to the equation of Shishkina et al. (2014) for a pressure of 500 MPa. While the overall exponential trend described by Shishkina et al. (2014) is generally observed, our experiments show higher CO_2 solubility than what the Shishkina et al. (2014) model predicts for these compositions. Additionally, compositions with nearly equivalent Π* sometimes display a wide range of CO_2 solubilities and, similar to the Dixon (1997) model, the Shishkina et al. (2014) model cannot account for differences in solubility at a single Π* value.

Another example of an empirical expression for CO_2 solubility in alkali-rich magmas is from the work of Vetere et al. (2014). Rather than fitting the data using cation fraction relationships like Dixon (1997) and Shishkina et al. (2014), the Vetere et al. (2014) study incorporated an additional compositional factor, the ratio of non-bridging oxygens to tetrahedrally coordinated cations (NBO/T). However, their focus was less comprehensive, defining the solubility of relatively polymerized and very alkali-rich magmas at 500 MPa. While the Vetere et al. (2014) equation is valid

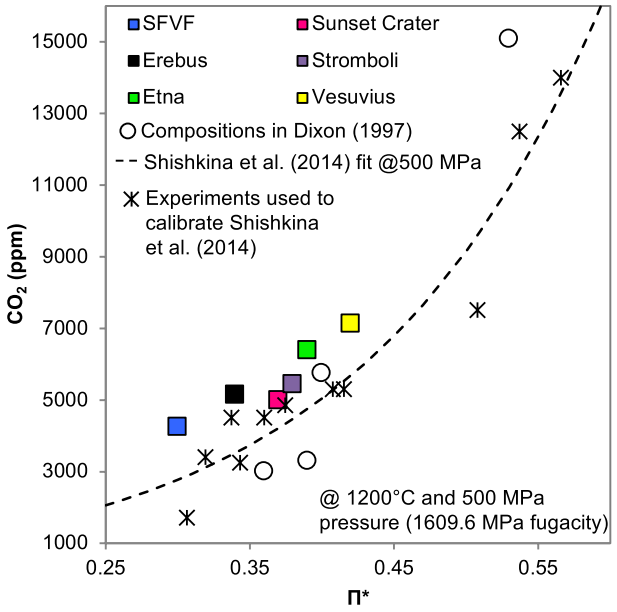

Fig. 8 Comparison of solubility for the six compositions in this study (squares) at 500 MPa to Π^* parameter (Shishkina et al. 2014). CO_2 concentrations at 500 MPa are calculated by power law fits through the experimental data (Eqs. 2-7). Also included are the Π^* values and CO_2 concentrations at 500 MPa for the four compositions discussed in Dixon (1997), shown as circles. Dashed curve represents solubilities predicted by Shishkina et al. (2014) model; the asterisks indicate the experiments that were utilized to calibrate the model

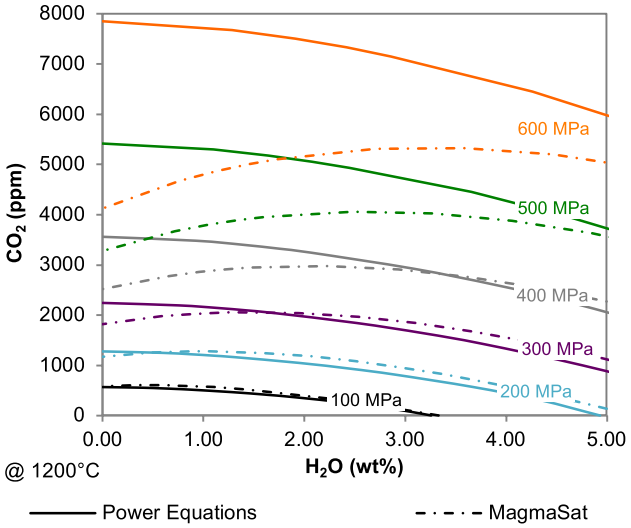

Fig. 9 Comparison of mixed-fluid (H_2O-CO_2) solubility of Stromboli with values calculated using MagmaSat (dashed curves; Ghiorso and Gualda 2015). The fluid-saturated isobars for the Stromboli composition are calculated using the empirical power fit for CO_2, Eq. 2 from this study and for H_2O, the Stromboli equation from Lesne et al. (2011a). Note that the MagmaSat model includes an effect of reduced CO_2 solubility at low H_2O conditions, which was not studied in these new experiments. Misfits between the isobars at low H_2O conditions are due to the inclusion of this possible effect in the MagmaSat model

for the Erebus composition, it is not calibrated for the full range of magmas in this study, and we therefore do not test it against our data.

Comparable to the Dixon (1997) and Lesne et al. (2011b) semi-empirical thermodynamic approach for H_2O–CO_2 solubility is the work of Iacono-Marziano et al. (2012). Instead of using the Π parameter, the Iacono-Marziano et al. (2012) model utilized a multi-parameter approach. Like the Vetere et al. (2014) model, the Iacono-Marziano et al. (2012) model incorporates a structural parameter in the form of NBO/O.

A comprehensive thermodynamic model

A few comprehensive thermodynamic models exist to calculate the volatile solubility for a wide range of compositions (basalt to rhyolite) over a large pressure range, including the models of Papale et al. (2006), Duan (2014), and Ghiorso and Gualda (2015). The MagmaSat model (Ghiorso and Gualda 2015) is one of the latest comprehensive models developed to describe all natural magmas across a very large pressure range (0–3 GPa). MagmaSat utilizes a full multicomponent thermodynamic approach, but because it incorporates experiments from the existing literature, it is not yet calibrated at the specific pressures and compositional range of interest here (refer to Fig. 1). This difference is illustrated in Fig. 9, which compares two sets of fluid-saturated isobars for the Stromboli composition. One set of isobars is calculated using MagmaSat, while the other uses power law fits for each volatile phase: Eq. 2 from this study for CO_2 and the equation from Lesne et al. (2011a) for water. The isobars, specifically CO_2 abundance at moderate (2 wt%) to high H_2O content, show good agreement below ~ 300 MPa. As pressure increases to 600 MPa, the MagmaSat model diverges significantly from the isobars fit to the new data. At lower H_2O abundance, the MagmaSat model shows non-Henrian behavior, with CO_2 solubility decreasing as H_2O abundance decreases. Our experiments, which all contain > 2 wt% H_2O, do not show this effect.

Water solubility

Lesne et al. (2011a) presented experiments focused on H_2O solubility in alkali-rich mafic magmas. All three compositions (Vesuvius, Etna, and Stromboli) in Lesne et al. (2011a) yielded similar water solubilities. Overall, the H_2O solubilities determined in Lesne et al. (2011a) trend with total alkali contents. The highest H_2O content correlates with highest alkalis, so H_2O solubility increases from Stromboli to Etna and is highest in the Vesuvius composition. However, this difference in water solubility is not greatly pronounced, and in fact the three compositions overlap in some experiments of equal pressure (Lesne et al. 2011a). At a total H_2O

pressure of 300 MPa, the calculated difference between water solubility of the Vesuvius and Stromboli compositions is less than 0.5 wt%, which represents ~ 7% relative difference. The power law fit for water solubility in the Etna composition from Lesne et al. (2011a):

$$f_{H_2O}^{1200^\circ C} = 104.98 * \text{wt\% } H_2O^{1.83}, \quad (8)$$

where f_{H_2O} is the H_2O fugacity, is plotted with the experiments from this study in Fig. 5. The new experiments generally show good agreement with this power law relationship.

The water data are required to accurately determine CO_2 solubility in alkali-rich mafic magmas, but it is not the primary topic of this study. Water solubility has already been well constrained in the Lesne et al. (2011a) study between ~ 1 and 6.5 wt% H_2O in three alkali-rich mafic compositions. The experiments in this study were not designed to describe water solubility in these magmas, so in some compositions there is not a very wide range in water contents across experiments of different pressures. The low $X_{H_2O}^f$ values of our experiments additionally complicate our water data because any error in the fluid fraction is exaggerated in the water fugacity, but is insignificant in the CO_2 fugacity. Therefore, we will not provide updated water solubilities for these compositions and instead rely on the Lesne et al. (2011a) model for water to define H_2O solubility in these magmas.

Calibration of a thermodynamic model for CO_2 solubility

The purely empirical fits we have provided thus far have their limitations, and one concern is that this type of model will be inaccurate when extrapolated to higher pressures. Thermodynamic models are preferred for this reason, and the necessary parameters can be derived from well-constrained solubility experiments. We therefore proceed by characterizing CO_2 solubility using the thermodynamic model described by Fine and Stolper (1986), Stolper and Holloway (1988), Dixon et al. (1995), and Lesne et al. (2011b). In this model, because CO_2 is stored in the melt as CO_3^{2-}, CO_2 solubility is defined by the reaction:

$$CO_2(\text{vapor}) + O^{2-}(\text{melt}) = CO_3^{2-}(\text{melt}), \quad (9)$$

with an equilibrium constant (at P and T) given by:

$$K(P,T) = \frac{a^m_{CO_3^{2-}}(P,T)}{a^m_{O^{2-}} * f_{CO_2}(P,T)}. \quad (10)$$

Assuming ideal mixing between CO_3^{2-} and O^{2-} (Stolper et al. 1987), the activity terms in Eq. 10 are replaced by mole fractions, and after manipulation (e.g., Holloway and Blank 1994), the effect of pressure and temperature on equilibrium (K) is given by:

$$K(P,T) = K_0(P_0, T_0) * \exp\left\{ -\int_{P_0}^{P} \frac{\Delta V_r^{0,m}}{RT} dP + \int_{T_0}^{T} \frac{\Delta H_r^0(T,P_0)}{RT^2} dT \right\}. \quad (11)$$

In Eq. 11, K_0 (P_0, T_0) is the equilibrium constant at the reference pressure and temperature, 1000 bar and 1200 °C. $\Delta V_r^{0,m}$ is the volume change of the condensed components of the reaction in Eq. 9:

$$\Delta V_r^{0,m} = V^{0,m}_{CO_3^{2-}} - V^{0,m}_{O^{2-}}, \quad (12)$$

where $V^{0,m}_{CO_3^{2-}}$ and $V^{0,m}_{O^{2-}}$ represent the molar volumes of the melt species in their standard states. ΔH_r^0 is the enthalpy change of the reaction in Eq. 9, but because we did not investigate CO_2 solubility at different temperatures, we do not consider the temperature-dependent integral in Eq. 11 and cannot provide constraints on ΔH_r^0.

The parameters $\Delta V_r^{0,m}$ and $K_0(P_0, T_0)$ can be empirically determined for each composition using data from experiments at a constant temperature. Equation 11 can be manipulated such that on a linear regression of $\ln\left[f_{CO_2}(P,T) * (X^m_{CO_2})^{-1}\right]$ versus $[(P - P_0)\,(RT)^{-1}]$, where $X^m_{CO_2}$ is the mole fraction of total CO_2 contents dissolved in the melt, the slope of this regression yields $\Delta V_r^{0,m}$ and y-intercept corresponds to $-\ln K_0$. Note that in this determination, pressure is in bars, and for a mixed H_2O–CO_2 experiment, the pressure (P) is the partial pressure due to CO_2 as determined from the CO_2 fugacity.

We calculate the thermodynamic parameters $\Delta V_r^{0,m}$ and K_0 (P_0, T_0) using this linear regression technique for each of the six compositions in this study (Table 4). This determination is dependent on high-pressure data (Holloway and Blank 1994), and so it is well suited to our dataset. For certain compositions, we incorporate lower-pressure experiments from other authors when available (refer to supplementary material). We include data from Lesne et al. (2011b) after recalculating the CO_2 contents and fugacities, as described in "Results", for appropriate comparison with our data. For the Etna composition, we also utilize some experiments from Iacono-Marziano et al. (2012). We included experiments from these additional datasets with fluid compositions > 0.1 $X_{H_2O}^f$ and CO_2 abundances > 175 ppm. An example of this regression is shown in Fig. 10 for the Etna and Stromboli compositions. The Etna composition is exceptionally well constrained as a result of multiple experimental studies using this composition (see Table 4; Fig. 10).

To calculate CO_2 solubility from Eq. 11, we follow the steps outlined in Holloway and Blank (1994), briefly reproduced here. We first calculate K (P, T) using Eq. 11 with the values of $\Delta V_r^{0,m}$ and K_0 as determined above. Next, we

Table 4 Thermodynamic parameters, $\Delta V_r^{0,m}$ and ln K_0, as determined from linear regressions (see Fig. 10) of experimental data

Composition	$\Delta V_r^{0,m}$	ln K_0	R^2	n	Cation fractions[a]						
					Si^{4+}	Al^{3+}	Na^{+}	K^{+}	Ca^{2+}	Mg^{2+}	Fe^{2+}*
Sunset Crater	16.40	− 14.67	0.91	3	0.438	0.176	0.061	0.009	0.097	0.119	0.085
SFVF	15.02	− 14.87	0.99	4	0.488	0.188	0.061	0.018	0.091	0.081	0.061
Erebus	15.83	− 14.65	0.92	3	0.436	0.204	0.107	0.033	0.068	0.045	0.080
Vesuvius	24.42	− 14.04	0.98	7	0.450	0.166	0.035	0.069	0.115	0.092	0.063
Etna	21.59	− 14.28	0.99	19	0.438	0.176	0.062	0.020	0.113	0.093	0.081
Stromboli	14.93	− 14.68	0.97	6	0.449	0.182	0.044	0.023	0.123	0.107	0.063

The number of experiments included in the regression for each composition (n) and the R^2 value of the fit are also listed. The cation fractions included here are used to calculate Π (after correction of Fe^{2+} for an oxygen fugacity of NNO + 1) and Π* (using Fe total = Fe^{2+} as listed)

*Fe^{2+} calculated from total iron expressed as FeO

[a]Cation fractions were calculated from anhydrous wt% according to the following formula: (wt%/formula weight) × (# cations in molecule), and then normalized to one. Ti^{4+}, Mn^{2+}, and P^{5+} were included, but are not reported

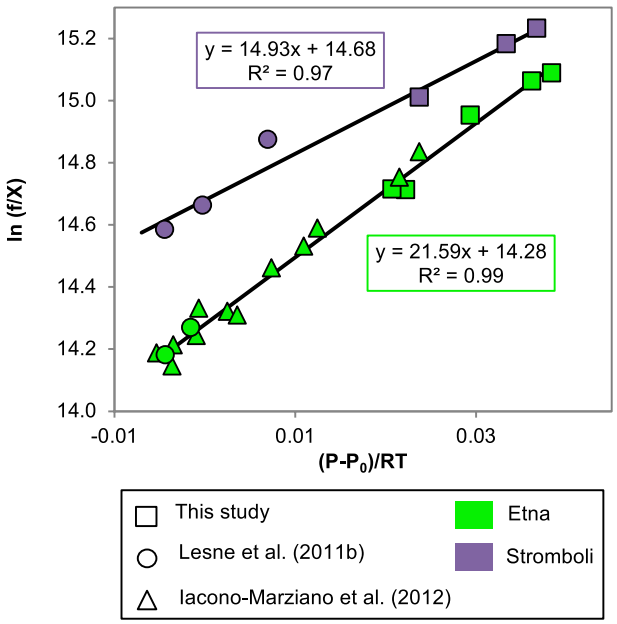

Fig. 10 Determination of thermodynamic parameters for the Etna and Stromboli compositions. The terms f and X correspond to the CO_2 fugacity and the mole fraction of CO_2 dissolved in the melt ($X^m_{CO_2}$), respectively. The slope of a linear regression of the data represents the partial molar volume ($\Delta V_r^{0,m}$) and the y-intercept represents the inverse value of ln K_0

calculate f_{CO_2} using the modified Redlich–Kwong equation of state (Holloway 1981, 1987; Holloway and Blank 1994) with the Saxena and Fei (1987) high-pressure correction. We use these values of $K(P, T)$ and f_{CO_2} to calculate a term K_f:

$$K_f = K(P, T) * f_{CO_2}(P, T). \tag{13}$$

$X^m_{CO_3^{2-}}$ is calculated from K_f:

$$X^m_{CO_3^{2-}} = K_f * (1 - K_f)^{-1}, \tag{14}$$

and this is converted to wt% CO_2 by:

$$\text{wt\% } CO_2 = \left(44.01 * X^m_{CO_3^{2-}}\right) * \left[\left(44.01 * X^m_{CO_3^{2-}}\right) + \left(1 - X^m_{CO_3^{2-}}\right) * \text{FW}_{\text{one}}\right]^{-1}, \tag{15}$$

where FW_{one} is the formula weight of the magma on a one-oxygen basis. To make the application of this model more straightforward, we assume the value of FW_{one} to be a constant, using the value given by Holloway and Blank (1994) for alkali basalt of 36.594. Values of FW_{one} calculated for our six compositions range within ± 1 of this alkali basalt value. The CO_2 solubility curves calculated for each composition using the thermodynamic model (Fig. 11) show strong agreement with the experimental data.

An Excel spreadsheet is included in the supplementary material to calculate fluid-saturated isobars, isopleths, and melt inclusion saturation pressures using the individual thermodynamic models for each composition.

Compositional influence on CO_2 solubility

Total alkali content

Several studies have shown that in mafic magmas, there is a general correlation between total alkali abundance and CO_2 solubility (e.g., Dixon 1997; Lesne et al. 2011b). In our new experiments, however, CO_2 solubility does not uniformly scale with total alkali content. There is significant overlap in solubility between the Sunset Crater, Stromboli, and Erebus compositions that have total alkali contents of 4.22 wt%, 4.55 wt%, and 8.81 wt%, respectively. Notably, the Erebus composition has the highest total alkali content of all compositions (8.81 wt%), and yet both the Etna (5.20 wt%) and Vesuvius (7.79 wt%) compositions have higher CO_2

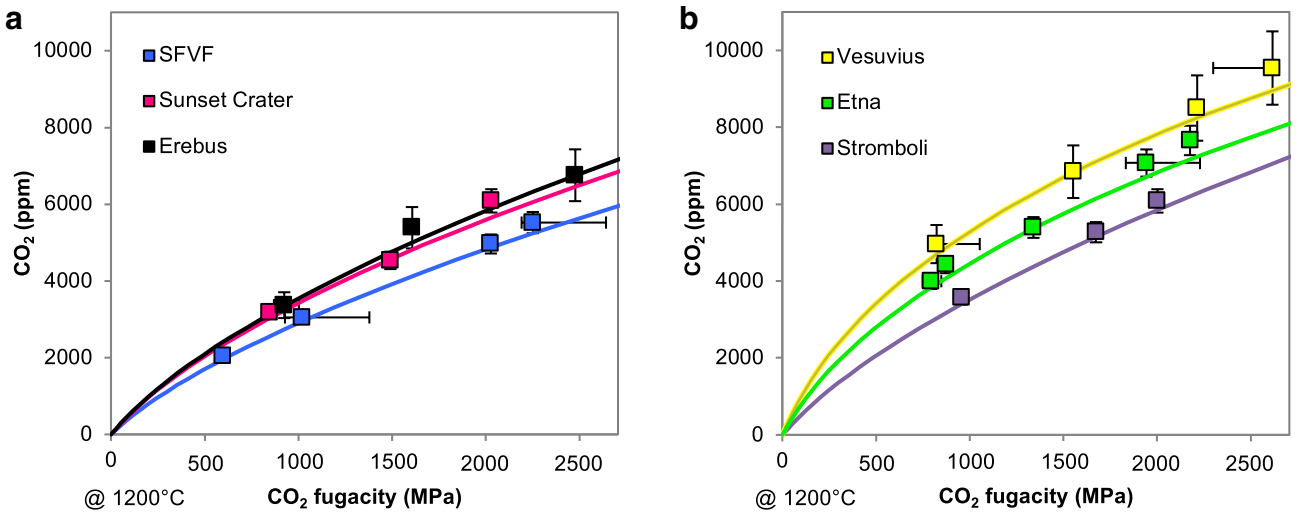

Fig. 11 Dissolved CO_2 concentration versus experimental CO_2 fugacity (squares; Table 2). Curves are calculated using the thermodynamic model and the respective experimentally determined parameters for each composition (Table 4)

solubilities. Interestingly, though the Vesuvius and Erebus compositions share similar total alkali contents, the Vesuvius magma has more potassium than sodium, whereas the reverse is true for Erebus. Based on these results, elements other than the alkalis do appear to play a role in CO_2 solubility in mafic magmas, and sodium and potassium likely do not share an equal influence (e.g., Vetere et al. 2014).

Comparison of elemental influences

In Fig. 12, we compare three of the experimental compositions (Etna, Sunset Crater, and Erebus) to identify elemental influence on CO_2 solubility (cation fractions; Table 4). A negative cation fraction difference represents a higher concentration of the element in the Etna composition, while a positive difference represents higher concentrations in the composition represented by the symbols. The Sunset Crater and Etna compositions are very similar in composition, with the exception of higher Mg^{2+} and lower Ca^{2+} and K^{+} contents in the Sunset Crater magma. If these three elements contribute equally to increase CO_2 solubility due to their role as structural modifiers, we would expect the solubilities of these magmas to be approximately equal, because the sum of the magnitude of their differences is essentially

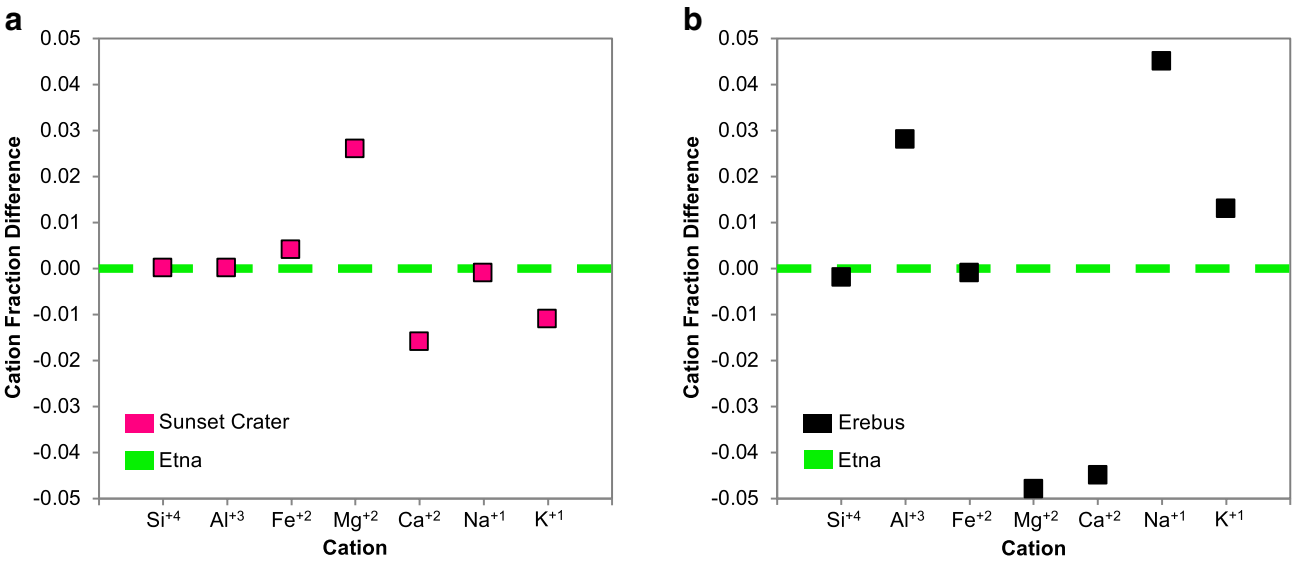

Fig. 12 Compositional comparison of Etna, Sunset Crater and Erebus (expressed as cation fraction; refer to Table 4). Note that positive differences indicate higher concentrations in the compositions represented by the symbols, and negative differences indicate higher concentrations in the Etna composition. The Etna composition has a higher CO_2 solubility than both Sunset Crater and Erebus

zero. Instead, we see that CO_2 solubility is roughly 15% higher in the Etna composition. We can therefore conclude that magnesium has a smaller effect on CO_2 solubility than calcium and potassium. This comparison also seems to reveal that CO_2 solubility is sensitive to small compositional differences. The calcium content, which is likely the most significant of the three elements (e.g., Spera and Bergman 1980; Dixon 1997), varies by less than 15% (1.8 wt%).

The Erebus case is more difficult to draw simple conclusions from, as it varies from the Etna composition in five of the seven major elements shown. However, this comparison does provide some clues as to how a composition with higher alkali content (Erebus) can have lower CO_2 solubility than a magma with lower alkali content (Etna). In this example, the solubility increase from the higher total alkali content in the Erebus composition could perhaps be negated by the effect of lower calcium and magnesium content and higher aluminum content compared to Etna, resulting in a lower CO_2 solubility for Erebus.

Evidence from the Π formulation

While the linear correlation of CO_2 solubility with Π (Dixon 1997) is not valid for our experimental data (see Fig. 6), the formulation of this parameter may still provide context for our experimental results. Dixon (1997) incorporated several observations on the effects of different elements on CO_2 solubility from previous studies (e.g., Mysen 1976; Spera and Bergman 1980) into the construction of the Π parameter. Cations were grouped in Π according to two factors: elements thought to reduce CO_2 solubility by promoting polymerization of the melt ($A = Si^{4+} + Al^{3+}$), and elements with the potential to increase CO_2 solubility due to their reaction with carbonate (termed "B", composed of Fe^{2+}, Mg^{2+}, Ca^{2+}, Na^+, and K^+). In the polymerization component of Π, Si^{4+} and Al^{3+} were given equal weighting. The cations that react with carbonate were ranked based on the Gibbs free energy (ΔG_r) of their carbonation reactions (Spera and Bergman 1980), and given a coefficient based on their ΔG_r value compared to that of Ca^{2+}. The resulting equation for the carbonate reaction component of Π is expressed by

$$B = Ca^{2+} + 0.8K^+ + 0.7Na^+ + 0.4\left(Fe^{2+} + Mg^{2+}\right), \quad (16)$$

which describes the net influence of these elements on CO_2 solubility (Dixon 1997).

Using the Π formulation to compare the solubility of different compositions yields additional insight into the compositional influence on CO_2 solubility. First, the general relationships of these elements, with Si^{4+} and Al^{3+} reducing CO_2 solubility, and Fe^{2+}, Mg^{2+}, Ca^{2+}, Na^+, and K^+ increasing CO_2 solubility, is consistent with our results. This can be seen in Fig. 6, as for these six compositions, a higher value of Π does yield higher CO_2 solubility. Specifically, for the compositions discussed in Fig. 12, the cation fractions in the Etna composition yield a higher value of B (Eq. 16) than both Sunset Crater and Erebus, and the composition also has less Si^{4+} and Al^{3+} (A) than Erebus. However, the magnitude of the relative contributions of each of these elements appears to be different from what is built into the Π formulation. The difference in Π value is much greater between Erebus and Etna than between Sunset Crater and Etna, yet the difference in solubility is identical. In order to constrain solubilities in these three compositions, the coefficients for the individual components of Π (A and B) would need to be altered from the original formulation so that the coefficient for B is smaller than the absolute value of the coefficient for A. However, we would not be able to describe the solubility of the Stromboli composition if the coefficient for B is smaller than the absolute value of the coefficient for A. A simple linear regression of A and B is therefore not possible within this compositional range.

These results indicate that there is a discrepancy in the formulation of Π and our current understanding of CO_2 solubility. The compositional elements do influence solubility as described by Dixon (1997), but the magnitude of Π does not directly correlate with solubility. There are a few possible compositional controls not currently accounted for in Π that could produce this discrepancy. First, it is probable that the contribution of aluminum is greater than that of silica, rather than contributing equally as in the current formula. When Al^{3+} forms a tetrahedron in the melt structure, it requires a metal cation such as Na^+ or K^+ to charge balance the AlO_4 molecule (e.g., Mysen et al. 1981). The aluminum therefore not only polymerizes the melt, but also removes the ability for one charge balancing cation to react with carbonate and store CO_2 in the melt. Second, there is perhaps another important compositional control on solubility missing from the formula. For example, the ratio of sodium to total alkalis has been useful in some models such as that of Vetere et al. (2014). It is possible that different carbonation reactions are preferred based on the relative proportions of alkali elements. One additional possibility is that the Gibbs free energy technique may not account for the full complexity of the melt structure. The relative contributions from Fe^{2+}, Mg^{2+}, Ca^{2+}, Na^+, and K^+ may not be consistent across all alkali-rich mafic compositions, possibly due to interaction between components. Well-calibrated, full multicomponent models are therefore likely required to accurately describe CO_2 solubility in a wide range of alkali-rich mafic magmas.

Other possible influences untested in this study

There is some evidence that the oxidation state of iron affects CO_2 solubility (e.g., Behrens et al. 2009), and some volatile solubility models account for variable f_{O_2}

(e.g., Papale et al. 2006; Duan 2014; Ghiorso and Gualda 2015). All of our experiments were conducted at relatively oxidizing conditions (~ NNO + 1). We therefore have not tried to incorporate the effect of iron speciation on volatile solubility.

Mysen (1976) found evidence that water increases CO_2 solubility in experiments run at pressures in excess of 2.5 GPa. Mysen (1976) hypothesized that this was due to the way in which H_2O and CO_2 fit into the melt pseudo-structure. These results, however, relied on the outdated beta-track analytical method. Subsequent studies conducted at low pressures utilizing infrared spectroscopy did not find any relationship between H_2O content and CO_2 solubility (e.g., Dixon et al. 1995). More recently, a number of studies have again found evidence for water influencing CO_2 solubility in basalt (e.g., Shishkina et al. 2010) and intermediate magmas (King and Holloway 2002), but the influence is currently poorly understood and unquantified (e.g., Iacono-Marziano et al. 2012; Shishkina et al. 2014). The MagmaSat model (Ghiorso and Gualda 2015), based on a survey of the experimental literature, does describe enhanced CO_2 solubility from low to moderate H_2O abundance. Our low $X^f_{H_2O}$ experiments have greater than 2 wt% dissolved H_2O and do not show a relationship between CO_2 solubility and water abundance. For this reason, we have not incorporated an H_2O influence on CO_2 solubility in our models.

Temperature may also strongly affect CO_2 solubility in alkali-rich mafic melts (e.g., Behrens et al. 2009), but its treatment varies in different models. Because all of our experiments were conducted at 1200 °C, we cannot comment on this possible effect on CO_2 solubility.

Implications for volcanism

Plumbing systems and melt inclusions

To demonstrate the impact of the new experimental data on melt inclusion interpretation and volcanic plumbing systems, we apply the new CO_2 solubility thermodynamic fits to samples from Stromboli from Métrich et al. (2010). The melt inclusions, from a historic large-scale paroxysm (ST531; fifteenth to seventeenth century A.D. eruption), contain between 624 and 1460 ppm CO_2 (Métrich et al. 2010). Saturation pressures were previously calculated using the Papale et al. (2006) model, yielding melt inclusion entrapment pressures between 105 and 206 MPa, with an average pressure of 176 MPa (Métrich et al. 2010). We recalculate CO_2 saturation from the thermodynamic model, using the parameters listed in Table 4 for Stromboli, and use the power law fit for Stromboli from Lesne et al. (2011a) for H_2O solubility. The resulting new entrapment pressures are between 144 and 257 MPa, with an average pressure of 220 MPa. The

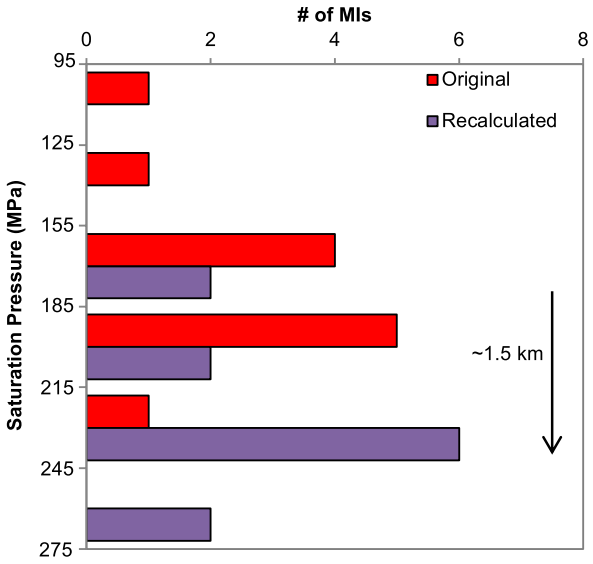

Fig. 13 Comparison of saturation pressures for melt inclusions (ST531 from Métrich et al. 2010) from Stromboli. Original pressures were calculated using the Papale et al. (2006) volatile solubility model in Métrich et al. (2010). Recalculated pressures use the thermodynamic fit for CO_2 in Table 4 and the H_2O power fit from Lesne et al. (2011a)

two sets of pressures are shown in the histogram in Fig. 13. The recalculated pressures are, on average, 44 MPa higher than the previous assessment, which indicates depths of melt inclusion entrapment approximately 1–2 km deeper than previously interpreted by Métrich et al. (2010). Calculations for the same melt inclusions using MagmaSat (Ghiorso and Gualda 2015) yield pressures between 139 and 249 MPa, with an average of 212 MPa. These pressures are closer to those calculated using our new model, although they are 8 MPa lower on average.

Physically, this means that we expect volatile exsolution to occur at deeper levels than previously estimated for this eruption, which may have played a role in the observed explosivity. Exsolved volatiles provide buoyancy to magma (e.g., Pyle and Pyle 1995; Woods and Cardoso 1997) and can generate overpressure in the magma storage zone (Blake 1984). Thus, if exsolution occurs deeper within the system, magma ascent and acceleration may also initiate at greater depths. This acceleration at depth could produce a feedback mechanism wherein fast magma ascent leads to volatile oversaturation in the melt, which then results in rapid volatile exsolution at shallower levels, driving highly explosive eruptions (e.g., Papale and Polacci 1999; Sable et al. 2006). Additionally, Métrich et al. (2010) note the presence of vapor bubbles in melt inclusions from Stromboli. These vapor bubbles may contain additional CO_2 (e.g., Hartley et al. 2014; Moore et al. 2015; Aster et al. 2016), signifying even greater depths of melt inclusion entrapment as well as

higher quantities of volatiles in the system that may facilitate explosive eruptions.

Magma ascent dynamics

Given the new experimental constraints on volatile solubility, it is possible to consider how the interaction between magma composition and solubility might impact the dynamics of magma ascent in alkali basalt compared to subalkaline basalt. Whereas low viscosity basaltic magmas often erupt mildly (e.g., Walker 1993), at least three of the alkali-rich mafic compositions investigated here (Stromboli, Sunset Crater, and Etna) have produced considerable explosive eruptions. Stromboli is known for persistent, small eruptive events, but also frequently generates more explosive paroxysms (Rosi et al. 2000). Sunset Crater produced a sub-Plinian eruption in 1085 A.D. (Amos 1986; Alfano et al. 2018), while Etna has a long history of explosive activity, including several sub-Plinian events (e.g., Coltelli et al. 2000) and at least one Plinian eruption (122 B.C.; Coltelli et al. 1998).

The solubility models developed here demonstrate that alkali-rich magmas associated with these explosive events should have high CO_2 solubility relative to subalkaline basalt. Assuming the abundance of volatiles available to the system is sufficient to achieve fluid saturation, at comparable depths, alkali-rich magma would have higher dissolved CO_2 contents than subalkaline basalt, potentially leading to more rapid ascent and more explosive eruptions. Alternatively, for magmas with similar dissolved volatile abundances (prior to reaching fluid saturation), the alkali-rich magmas would ascend to shallower depths than subalkaline basalts before becoming volatile saturated, thereby delaying the initiation of exsolution. This delay could lead to better coupling between magma and gas during ascent, again leading to more rapid ascent and/or shallower fragmentation, promoting more explosive eruptions. High CO_2 abundances have been associated with highly explosive basaltic eruptions (e.g., Allison 2018; Moretti et al. 2018), and our results suggest that such conditions are generally more likely to be achieved in alkali-rich systems. Comparison of clast textures (microlites and bubbles; e.g., Taddeucci et al. 2004; Sable et al. 2006; Cimarelli et al. 2010) might show whether alkali-rich magma systems, especially those associated with explosive events, generally differ from subalkaline basalts in terms of their ascent conditions.

Conclusions

Experiments at 1200 °C between 400 and 600 MPa with mixed fluid (H_2O–CO_2), were conducted to study CO_2 solubility in a variety of alkali-rich mafic magmas. The findings of this work are summarized below.

1. Mafic magmas rich in alkali elements show increased CO_2 solubilities, though the correlation is not a simple scaling with total alkali content.
2. Previous volatile solubility models for alkali-rich mafic magmas do not accurately describe CO_2 solubility at mid-crustal pressures (400 to 600 MPa). Discrepancies in solubilities have implications for the physical volcanic system, as solubility determines depths of volatile exsolution, which can drive explosive eruptions.
3. CO_2 solubility in alkali-rich mafic magmas is well constrained by a simple thermodynamic model using two parameters that can be derived from the experimental data. We have calibrated the thermodynamic model for six individual compositions ranging from alkali basalt to phonotephrite to basaltic andesite. These compositions include magmas from Stromboli, Etna, and Erebus volcanoes.
4. Comparison of compositionally similar magmas demonstrates how small variations in some elements significantly influence solubility. Experiments show that largely similar magmas from Etna and Sunset Crater have roughly 15% relative difference in their CO_2 solubility.
5. As has been suggested by several previous studies, CO_2 solubility in alkali-rich mafic magmas appears to be inversely correlated with Si^{4+} and Al^{3+} content, but positively correlated with Ca^{2+}, Na^{+}, and K^{+}. The effects of individual elements on CO_2 solubility are not well represented by comprehensive compositional parameters, and multicomponent models are likely necessary to describe this behavior.
6. When we apply the thermodynamic model for CO_2 solubility to melt inclusion data from Stromboli volcano, we calculate saturation pressures approximately 44 MPa higher than previous estimates. These higher pressures indicate greater depths of melt inclusion entrapment, requiring an adjustment to the interpretation of the complex plumbing system beneath Stromboli.
7. The enhanced CO_2 solubility of alkali-rich mafic magmas could contribute to explosive volcanism in two ways. First, assuming fluid saturation, alkali-rich magmas would have higher dissolved volatile contents than subalkaline magmas at similar pressures, resulting in larger volatile budgets. Second, comparing magmas with equal volatile contents that are not fluid-saturated, an alkali-rich magma will reach saturation at lower pressures compared to subalkaline magma, delaying volatile exsolution to shallow levels and possibly producing more explosive eruptions.

Acknowledgements This work was supported by the National Science Foundation Grants EAR-1322078 and EAR-1642569. We are

grateful to Jake Lowenstern (United States Geological Survey), Ken Domanik (University of Arizona), and Kurt Leinenweber (ASU) for assistance with analytical instruments and other equipment. We gratefully acknowledge the use of facilities at the LeRoy Eyring Center for Solid State Science at ASU. We thank two reviewers and editor Mark Ghiorso for their comments to improve this manuscript.

References

Alfano F, Ort MH, Pioli L, Self S, Hanson SL, Roggensack K, Allison CM, Amos R, Clarke AB (2018) Subplinian monogenetic basaltic eruption of Sunset Crater, Arizona, USA. Geol Soc Am Bull 131:661–674. https://doi.org/10.1130/B31905.1

Allison CM (2018) Highly explosive mafic volcanism: the role of volatiles. Ph.D. thesis, Arizona State University

Amos RC (1986) Sunset Crater, Arizona: evidence for a large magnitude Strombolian eruption. M.S. thesis, Arizona State University

Aster EM, Wallace PJ, Moore LR, Watkins J, Gazel E, Bodnar RJ (2016) Reconstructing CO_2 concentrations in basaltic melt inclusions using Raman analysis of vapor bubbles. J Volcanol Geotherm Res 323:148–162. https://doi.org/10.1016/j.jvolgeores.2016.04.028

Behrens H, Misiti V, Freda C, Vetere F, Botcharnikov RE, Scarlato P (2009) Solubility of H_2O and CO_2 in ultrapotassic melts at 1200 and 1250 degrees C and pressure from 50 to 500 MPa. Am Mineral 94:105–120. https://doi.org/10.2138/am.2009.2796

Blackburn EA, Wilson L, Sparks RSJ (1976) Mechanisms and dynamics of Strombolian activity. J Geol Soc (Lond UK) 132:429–440

Blake S (1984) Volatile oversaturation during the evolution of silicic magma chambers as an eruption trigger. J Geophys Res 89:8237–8244

Blank JG, Brooker RA (1994) Experimental studies of carbon dioxide in silicate melts: solubility, speciation, and stable carbon isotope behavior. In: Carroll MR, Holloway JR (eds) Volatiles in magmas, vol 30. Mineralogical Society of America, Washington, pp 157–186

Botcharnikov R, Freise M, Francois H, Behrens H (2005a) Solubility of C–O–H mixtures in natural melts: new experimental data and application range of recent models. Ann Geophys 48:633–646

Botcharnikov RE, Koepke J, Holtz F, McCammon C, Wilke M (2005b) The effect of water activity on the oxidation and structural state of Fe in a ferro-basaltic melt. Geochim Cosmochim Acta 69:5071–5085. https://doi.org/10.1016/j.gca.2005.04.023

Cimarelli C, Di Traglia F, Taddeucci J (2010) Basaltic scoria textures from a zoned conduit as precursors to violent Strombolian activity. Geology 38:439–442. https://doi.org/10.1130/G30720.1

Coltelli M, Del Carlo P, Vezzoli L (1998) Discovery of a Plinian basaltic eruption of Roman age at Etna volcano, Italy. Geology 26:1095–1098

Coltelli M, Del Carlo P, Vezzoli L (2000) Stratigraphic constraints for explosive activity in the past 100 ka at Etna volcano, Italy. Int J Earth Sci 89:665–677. https://doi.org/10.1007/s005310000117

Dixon JE (1997) Degassing of alkalic basalts. Am Mineral 82:368–378

Dixon JE, Pan V (1995) Determination of the molar absorptivity of dissolved carbonate in basanitic glass. Am Mineral 80:1339–1342

Dixon JE, Stolper EM (1995) An experimental study of water and carbon dioxide solubilities in mid-ocean ridge basaltic liquids. Part II: applications to degassing. J Petrol 36(6):1633–1646

Dixon JE, Stolper E, Delaney JR (1988) Infrared spectroscopic measurements of CO_2 and H_2O in Juan de Fuca Ridge basaltic glasses. Earth Planet Sci Lett 90:87–104

Dixon JE, Stolper EM, Holloway JR (1995) An experimental study of water and carbon dioxide solubilities in mid ocean ridge basaltic liquids. Part I: calibration and solubility models. J Petrol 36(6):1607–1631

Duan X (2014) A general model for predicting the solubility behavior of H_2O–CO_2 fluids in silicate melts over a wide range of pressure, temperature and compositions. Geochim Cosmochim Acta 125:582–609. https://doi.org/10.1016/j.gca.2013.10.018

Fine G, Stolper E (1986) Dissolved carbon dioxide in basaltic glasses: concentration and speciation. Earth Planet Sci Lett 76:263–278

Ghiorso MS, Gualda GAR (2015) An H_2O–CO_2 mixed fluid saturation model compatible with rhyolite-MELTS. Contrib Mineral Petrol 169:53. https://doi.org/10.1007/s00410-015-1141-8

Hartley ME, Maclennan J, Edmonds M, Thordarson T (2014) Reconstructing the deep CO_2 degassing behaviour of large basaltic fissure eruptions. Earth Planet Sci Lett 393:120–131. https://doi.org/10.1016/j.epsl.2014.02.031

Hess KU, Dingwell DD (1996) Viscosities of hydrous leucogranitic melts: a non-Arrhenian model. Am Mineral 81:1297–1300. https://doi.org/10.2138/am-1996-9-1031

Holloway JR (1981) Volatile interactions in magmas. In: Newton RC, Navrotsky A, Wood BJ (eds) Thermodynamics of minerals and melts. Springer, New York, pp 273–293

Holloway JR (1987) Igneous fluids. Rev Mineral Geochem 17(1):211–232

Holloway JR, Blank JG (1994) Application of experimental results to C–O–H species in natural melts. In: Carroll MR, Holloway JR (eds) Volatiles in magmas, vol 30. Mineralogical Society of America, Washington, pp 187–230

Iacono-Marziano G, Morizet Y, Le Trong E, Gaillard F (2012) New experimental data and semi-empirical parameterization of H_2O–CO_2 solubility in mafic melts. Geochim Cosmochim Acta 97:1–23. https://doi.org/10.1016/j.gca.2012.08.035

Iacovino K, Moore G, Roggensack K, Oppenheimer C, Kyle P (2013) H_2O–CO_2 solubility in mafic alkaline magma: applications to volatile sources and degassing behavior at Erebus volcano, Antarctica. Contrib Mineral Petrol 166:845–860. https://doi.org/10.1007/s00410-013-0877-2

Iacovino K, Oppenheimer C, Scaillet B, Kyle P (2016) Storage and evolution of mafic and intermediate alkaline magmas beneath Ross Island, Antarctica. J Petrol 57(1):93–118. https://doi.org/10.1093/petrology/egv083

Kilinc A, Carmichael ISE, Rivers ML, Sack RO (1983) The ferric-ferrous ratio of natural silicate liquids equilibrated in air. Contrib Mineral Petrol 83:136–140

King PL, Holloway JR (2002) CO_2 solubility and speciation in intermediate (andesitic) melts: the role of H_2O and composition. Geochim Cosmochim Acta 66(9):1627–1640

Lesne P, Scaillet B, Pichavant M, Iacono-Marziano G, Beny JM (2011a) The H_2O solubility of alkali basalts: an experimental study. Contrib Mineral Petrol 162(1):133–151. https://doi.org/10.1007/s00410-010-0588-x

Lesne P, Scaillet B, Pichavant M, Beny JM (2011b) The carbon dioxide solubility in alkali basalts: an experimental study. Contrib Mineral Petrol 162(1):153–168. https://doi.org/10.1007/s00410-010-0585-0

Lowenstern JB (1995) Applications of silicate-melt inclusions to the study of magmatic volatiles. In: Thompson JFH (ed) Magmas, fluids and ore deposition, vol 23. Mineralogical Association of Canada, Short Course, Quebec, pp 71–99

Luhr JF (2001) Glass inclusions and melt volatile contents at Parícutin Volcano, Mexico. Conrib Mineral Petrol 142:261–283. https://doi.org/10.1007/s004100100293

Mandeville CW, Webster JD, Rutherford MJ, Taylor BE, Timbal A, Faure K (2002) Determination of molar absorptivities for infrared absorption bands of H_2O in andesitic glasses. Am Mineral 87:813–821. https://doi.org/10.2138/am-2002-0702

Manga M, Castro J, Cashman KV, Loewenberg M (1998) Rheology of bubble-bearing magmas. J Volcanol Geotherm Res 87:15–28

Métrich N, Bertagnini A, Di Muro A (2010) Conditions of magma storage, degassing, and ascent at Stromboli: new insights into the volcano plumbing system with inferences on the eruptive dynamics. J Petrol 51:603–626. https://doi.org/10.1093/petrology/egp083

Moore G (2008) Interpreting H_2O and CO_2 contents in melt inclusions: constraints from solubility experiments and modeling. In: Putirka KD, Tepley FJ (eds) Minerals, inclusions and volcanic processes, vol 69. Mineralogical Society of America, Washington, pp 333–361. https://doi.org/10.2138/rmg.2008.69.9

Moore G, Carmichael ISE (1998) The hydrous phase equilibria (to 3 kbar) of an andesite and basaltic andesite from western Mexico: constraints on water content and conditions of phenocryst growth. Contrib Mineral Petrol 130:304–319

Moore G, Roggensack K, Klonowski S (2008) A low-pressure–high-temperature technique for the piston-cylinder. Am Mineral 93:48–52. https://doi.org/10.2138/am.2008.2618

Moore LR, Gazel E, Tuohy R, Lloyd AS, Esposito R, Steele-MacInnis M, Hauri EH, Wallace PJ, Plank T, Bodnar RJ (2015) Bubbles matter: an assessment of the contribution of vapor bubbles to melt inclusion volatile budgets. Am Mineral 100:806–823. https://doi.org/10.2138/am-2015-5036

Moretti R, Métrich N, Arienzo I, Di Renzo V, Aiuppa A, Allard P (2018) Degassing vs. eruptive styles at Mt. Etna volcano (Sicily, Italy). Part I: volatile stocking, gas fluxing, and the shift from low-energy to highly explosive basaltic eruptions. Chem Geol 482:1–17. https://doi.org/10.1016/j.chemgeo.2017.09.017

Mysen BO (1976) The role of volatiles in silicate melts: solubility of carbon dioxide and water in feldspar, pyroxene, and feldspathoid melts to 30 kb and 1625 °C. Am J Sci 276:969–996

Mysen BO, Virgo D, Kushiro I (1981) The structural role of aluminum in silicate melts–a Raman spectroscopic study at 1 atmosphere. Am Mineral 66:678–701

Newman S, Lowenstern JB (2002) VOLATILECALC: a silicate melt-H_2O–CO_2 solution model written in Visual Basic for excel. Comput Geosci 28(5):597–604. https://doi.org/10.1016/S0098-3004(01)00081-4

Nichols ARL, Wysoczanski RJ (2007) Using micro-FTIR spectroscopy to measure volatile contents in small and unexposed inclusions hosted in olivine crystals. Chem Geol 242:371–384. https://doi.org/10.1016/j.chemgeo.2007.04.007

Ochs FA, Lange RA (1999) The density of hydrous magmatic liquids. Science 283:1314–1317

Ohlhorst S, Behrens H, Holtz F (2001) Compositional dependence of molar absorptivities of near-infrared OH- and H_2O bands in rhyolitic to basaltic glasses. Chem Geol 174:5–20. https://doi.org/10.1016/S0009-2541(00)00303-X

Pan V, Holloway JR, Hervig RL (1991) The pressure and temperature dependence of carbon dioxide solubility in tholeiitic basalt melts. Geochim Cosmochim Acta 55:1587–1595

Papale P, Polacci M (1999) Role of carbon dioxide in the dynamics of magma ascent in explosive eruptions. Bull Volcanol 60:583–594

Papale P, Moretti R, Barbato D (2006) The compositional dependence of the saturation surface of $H_2O + CO_2$ fluids in silicate melts. Chem Geol 229:78–95. https://doi.org/10.1016/j.chemgeo.2006.01.013

Pichavant M, Di Carlo I, Le Gac Y, Rotolo SG, Scaillet B (2009) Experimental constraints on the deep magma feeding system at Stromboli volcano, Italy. J Petrol 50(4):601–624. https://doi.org/10.1093/petrology/egp014

Pichavant M, Scaillet B, Pommier A, Iacono-Marziano G, Cioni R (2014) Nature and evolution of primitive Vesuvius magmas: an experimental study. J Petrol 55(11):2281–2310. https://doi.org/10.1093/petrology/egu057

Pyle DM, Pyle DL (1995) Bubble migration and the initiation of volcanic eruptions. J Volcanol Geotherm Res 67:227–232

Rosi M, Bertagnini A, Landi P (2000) Onset of the persistent activity at Stromboli volcano (Italy). Bull Volcanol 62:294–300. https://doi.org/10.1007/s004450000098

Sable JE, Houghton BF, Del Carlo P, Coltelli M (2006) Changing conditions of magma ascent and fragmentation during the Etna 122 BC basaltic Plinian eruption: evidence from clast microtextures. J Volcanol Geotherm Res 158:333–354. https://doi.org/10.1016/j.jvolgeores.2006.07.006

Saxena SK, Fei Y (1987) High pressure and high temperature fluid fugacities. Geochim Cosmochim Acta 51:783–791

Schrader B (1995) Infrared and Raman spectroscopy: methods and applications. VCH, Weinheim

Shishkina TA, Botcharnikov RE, Holtz F, Almeev RR, Portnyagin MV (2010) Solubility of H_2O- and CO_2-bearing fluids in tholeiitic basalts at pressures up to 500MPa. Chem Geol 277:115–125. https://doi.org/10.1016/j.chemgeo.2010.07.014

Shishkina TA, Botcharnikov RE, Holtz F, Almeev RR, Jazwa AM, Jakubiak AA (2014) Compositional and pressure effects on the solubility of H_2O and CO_2 in mafic melts. Chem Geol 388:112–129. https://doi.org/10.1016/j.chemgeo.2014.09.001

Sparks RSJ (1978) The dynamics of bubble formation and growth in magmas: a review and analysis. J Volcanol Geotherm Res 3:1–37

Spera FJ, Bergman SC (1980) Carbon dioxide in igneous petrogenesis: i. aspects of the dissolution of CO_2 in silicate liquids. Contrib Mineral Petrol 74:55–66

Stolper E, Holloway JR (1988) Experimental determination of the solubility of carbon dioxide in molten basalt at low pressure. Earth Planet Sci Lett 87:397–408

Stolper E, Fine G, Johnson T, Newman S (1987) Solubility of carbon dioxide in albitic melt. Am Mineral 72:1071–1085

Taddeucci J, Pompilio M, Scarlato P (2004) Conduit processes during the July–August 2001 explosive activity of Mt. Etna (Italy): inferences from glass chemistry and crystal size distribution of ash particles. J Volcanol Geotherm Res 137:33–54. https://doi.org/10.1016/j.jvolgeores.2004.05.011

Thibault Y, Holloway JR (1994) Solubility of CO_2 in a Ca-rich leucitite: effects of pressure, temperature, and oxygen fugacity. Contrib Mineral Petrol 116:216–224

Vetere F, Holtz F, Behrens H, Botcharnikov RE, Fanara S (2014) The effect of alkalis and polymerization on the solubility of H_2O and CO_2 in alkali-rich silicate melts. Contrib Mineral Petrol 167:1014. https://doi.org/10.1007/s00410-014-1014-6

Von Aulock FW, Kennedy BM, Schipper CI, Castro JM, Martin DE, Oze C, Watkins JM, Wallace PJ, Puskar L, Bégué F, Nichols ARL, Tuffen H (2014) Advance in Fourier transform infrared spectroscopy of natural glasses: from sample preparation to data analysis. Lithos 206–207:52–64. https://doi.org/10.1016/j.lithos.2014.07.017

Walker GPL (1993) Basaltic-volcano systems. In: Prichard HM, Alabaster T, Harris NBW, Neary CR (eds) Magmatic processes and plate tectonics, vol No 76. Geological Society Special Publication, London, pp 3–38

Wilson L (1980) Relationships between pressure, volatile content and ejecta velocity in three types of volcanic explosion. J Volcanol Geotherm Res 8:297–313

Wilson L, Head JW III (1981) Ascent and eruption of basaltic magma on the Earth and Moon. J Volcanol Geotherm Res 86:2971–3001

Wilson L, Sparks RSJ, Walker GPL (1980) Explosive volcanic eruptions – IV. The control of magma properties and conduit geometry on eruption column behavior. Geophys J Int 63:117–148. https://doi.org/10.1111/j.1365-246X.1980.tb02613.x

Witham F, Blundy J, Kohn SC, Lesne P, Dixon J, Churakov SV, Botcharnikov R (2012) SolEx: a model for mixed COHSCl-volatile solubilities and exsolved gas compositions in basalt. Comput Geosci 45:87–97. https://doi.org/10.1016/j.cageo.2011.09.021

Woods AW, Cardoso SSS (1997) Triggering basaltic volcanic eruptions by bubble-melt separation. Nature 385:518–520

Wyllie PJ, Tuttle OF (1959) Effect of carbon dioxide on the melting of granite and feldspars. Am J Sci 257:618–655